Nature Communications

https://doi.org/10.1038/s41467-026-71426-8

Article in Press

Distinct modes of dopamine modulation on striatopallidal synaptic transmission

Received: 4 April 2025

Accepted: 20 March 2026

Cite this article as: Lee, Y.L., Reva, M., Kim, K.J. *et al.* Distinct modes of dopamine modulation on striatopallidal synaptic transmission. *Nat Commun* (2026). https://doi.org/10.1038/s41467-026-71426-8

Youngeun Lina Lee, Maria Reva, Ki Jung Kim, Hyun-Jin Kim, Yemin Kim, Eunjeong Cho, Minseok Jeong, Youngjong Kwak, Kyungjae Myung, Yulong Li, Seung Eun Lee, Dong Pyo Jang, C. Justin Lee, Christian Lüscher & Jae-Ick Kim

Distinct modes of dopamine modulation on striatopallidal synaptic transmission

Youngeun Lina Lee[1], Maria Reva[2], Ki Jung Kim[3], Hyun-Jin Kim[1], Yemin Kim[1], Eunjeong Cho[1], Minseok Jeong[1], Youngjong Kwak[4], Kyungjae Myung[5,6], Yulong Li[7], Seung Eun Lee[8], Dong Pyo Jang[4], C. Justin Lee[3], Christian Lüscher[2,9], and Jae-Ick Kim[1*]

[1]Department of Biological Sciences, Ulsan National Institute of Science and Technology, Ulsan, Republic of Korea

[2]Department of Basic Neurosciences, Faculty of Medicine, University of Geneva, Geneva, Switzerland

[3]Center for Cognition and Sociality, Institute for Basic Science, Daejeon, Republic of Korea

[4]Department of Biomedical Engineering, Hanyang University, Seoul, Republic of Korea

[5]Center for Genomic Integrity, Institute for Basic Science, Ulsan, Republic of Korea

[6]Department of Biomedical Engineering, Ulsan National Institute for Science and Technology, Ulsan, Republic of Korea

[7]State Key Laboratory of Membrane Biology, Peking University School of Life Sciences, Beijing, China

[8]Research Animal Resource Center, Korea Institute of Science and Technology, Seoul, Republic of Korea

[9]Clinic of Neurology, Department of Clinical Neurosciences, Geneva University Hospital, Geneva, Switzerland

*Correspondence should be addressed to: jikim220@unist.ac.kr

Abstract

Dopamine affects voluntary movement by modulating basal ganglia function. However, the contribution of dopamine on striatopallidal synapses, an initial hub in the indirect pathway connecting the striatum to the GPe, remains poorly understood because of the sparse dopaminergic innervation. Here, we combine optogenetic projection targeting, whole cell patch clamp recordings in acute brain slices from mice, and computational modeling to overcome this limitation. We show that dopamine activates D2 receptors (D2Rs) and D4 receptors (D4Rs) differentially in distinct GPe subregions. In a pinwheel-like fashion, dorsolateral and ventromedial GPe expresses high levels of D2Rs, which exert presynaptic inhibition, while in dorsomedial and ventrolateral GPe D4Rs cause postsynaptic inhibition. Dopamine depletion by 6-OHDA reshapes the region-specific effect of dopamine, shifting it in the opposite direction and contributing to hypokinesia. These findings reveal the mechanism by which the different modality information conveyed spatially through the indirect pathway is differentially modulated by dopamine at striatopallidal synapses.

Introduction

The proper control of voluntary movement is vital for survival. The core brain regions modulating voluntary movement are the basal ganglia, a network of interconnected subcortical nuclei[1,2]. Sensory and motor information, widely distributed across the cortex, enters the basal ganglia, which contributes, among other functions, to select the appropriate motor strategy[3]. Central among these processes is the modulation of neuronal activity and synaptic transmission by the neuromodulator dopamine (DA) within the basal ganglia. The primary source of DA for goal-directed movement is the midbrain DA neurons located in the substantia nigra pars compacta (SNc), which predominantly innervate the striatum via the nigrostriatal pathway[4]. Within the striatum, the input nucleus of the basal ganglia, over 90% of neurons are GABAergic projection neurons known as medium spiny neurons (MSNs)[5]. Anatomically, the striatal MSNs can be categorized into two distinct groups: "direct" and "indirect" pathway MSNs. Interestingly, direct MSNs (dMSNs) projecting "directly" to the SNr/GPi (substantia nigra pars reticulata and internal globus pallidus, respectively), the primary output nuclei of the basal ganglia, express the DA D1 receptors (D1Rs), while indirect MSNs (iMSNs) projecting "indirectly" to the SNr/GPi by way of the external globus pallidus (GPe), express the DA D2 receptors (D2Rs)[1,2]. DA orchestrates the activity of MSNs through these receptors and the ensuing synaptic plasticity of excitatory afferents. In an action selection model, the direct pathway promotes appropriate motor strategies, whereas the indirect pathway suppresses other competing or inappropriate ones[3,4]. Consequently, the depletion of DA causes hyperactivity of the indirect pathway, resulting in an excessive inhibition of the thalamus and ultimately leading to the suppression of movement[5–7].

Striatopallidal synapses in the GPe, the first synaptic connection between nuclei of the indirect pathway, are a critical node where the axon terminals of extensively distributed iMSNs converge. Midbrain dopaminergic neurons, while predominantly projecting to the striatum, also give rise to collateral axons innervating the GPe[6,7]. However, studies to date have found only limited evidence supporting the functional significance of this innervation in modulating striatopallidal synaptic transmission[6,8–10]. On the other hand, it has been reported that the administration of DA or D2R agonists reduces striatopallidal GABAergic transmission with increased paired-pulse ratio (PPR), possibly attributable to the presence of presynaptic D2Rs at

striatopallidal axon terminals[8–10]. In addition, GPe neurons seem to express other D2-like receptors, including D4Rs[11,12], which may contribute to DA's postsynaptic effect at striatopallidal synapses[13]. Despite these findings, our understanding of the dopaminergic modulation of striatopallidal transmission in the GPe is still incomplete. Notably, midbrain DA neurons are not a monolith; they encompass molecularly and functionally heterogeneous populations that can innervate anatomically and spatially distinct compartments of the striatum and other basal ganglia nuclei. This characteristic of DA neurons and their axons may explain in part the fact that each subdivision of the striatum is involved in specific animal behaviors[12,13]. In a similar vein, recent findings suggest that the indirect pathway can maintain anatomically parallel subnetworks, and striatopallidal synapses, depending on their anatomical location within the GPe, may convey different modalities of information[14,15]. However, the majority of previous studies on the GPe have treated striatopallidal synapses as uniform in their physiological properties. Hence, whether dopaminergic modulation of synaptic transmission can vary by the anatomical location of striatopallidal synapses in the GPe remains to be elucidated.

Here, we sought to determine how dopaminergic modulation shapes striatopallidal synaptic transmission in the GPe. Our data demonstrated that dopaminergic axons originating from the midbrain innervate the GPe, exhibit region-specific distribution, and locally release dopamine. In addition, DA D2-like receptors could modulate striatopallidal synaptic transmission in a region-specific manner across different subdivisions of the GPe. Specifically, the activation of D2-like receptors resulted in an increased paired-pulse ratio (PPR) and a decrease in GABAergic transmission within the dorsolateral (DL) and ventromedial (VM) regions of the GPe. Surprisingly, this dopaminergic effect on PPR was absent in the ventrolateral (VL) and dorsomedial (DM) GPe, despite the observed reduction in GABAergic transmission in these areas.

In contrast, DA depletion reshaped the modulation of striatopallidal transmission by DA D2-like receptors in the GPe. 6-OHDA-induced DA depletion particularly promoted an increase in PPR in the VL and DM subregions of the GPe, while attenuating the rise in PPR in the DL and VM GPe. These results suggest that distinct sensory-motor information conveyed via the indirect pathway can be differentially modulated by DA, contingent upon the anatomical locations of striatopallidal synapses. Given that the structural and functional organization of basal ganglia circuits determines DA-related psychomotor functions and behaviors, our findings offer insights

into the previously overlooked role of dopaminergic modulation on striatopallidal synapses and globus pallidus in health and disease.

Results

DA axons capable of releasing DA innervate the GPe with regional heterogeneity

Although dopaminergic innervation of the GPe has been reported previously[6,7], direct evidence supporting local dopamine release from these axon terminals remains limited. We first examined the origin of dopaminergic axons innervating the GPe and found that the majority of TH-positive axons originated from SNc DA neurons[16,17] (Supplementary Fig. 1). Attempts to monitor DA transmission in the GPe using conventional electrochemical methods have been hindered by the sparse innervation of dopaminergic axon fibers to the GPe. However, recent advancements in fluorescent reporters for DA hold great promise for examining relatively weak DA transmission in brain regions such as the GPe[8,18,19]. To investigate whether dopaminergic axonal boutons innervating the GPe are functional and capable of releasing DA, we employed adeno-associated viruses (AAVs) encoding the genetically encoded fluorescent DA sensor $GRAB_{DA}$ (rDA2h)[20]. These AAVs were injected into the GPe, and DA release was monitored by changes in fluorescence intensity within the imaging area. To compare the relative amplitude of DA transmission across other DA-projecting regions, AAVs expressing the $GRAB_{DA}$ sensor were also injected into the M1 cortex and dorsolateral striatum (DLS). Three weeks post-injection, acute brain slices were prepared, and one-photon imaging combined with electrical stimulation was utilized to measure stimulus-evoked DA release. Although relatively small in amplitude compared to the DLS, electrical stimulation clearly evoked DA transmission in the GPe, indicating that DA axonal boutons in the GPe are functional and release DA (Fig. 1a,b). Consistently, fast-scan cyclic voltammetry (FSCV) measurements detected reliable evoked DA release in both the DLS (373.27 ± 40.15 nM) and GPe (14.27 ± 3.41 nM), confirming that dopaminergic terminals in the GPe are capable of releasing measurable amounts of DA (Supplementary Fig. 2a-c).

To further interrogate the innervation patterns of DA axons within the GPe subregions, we analyzed the regional variations of DA fibers by dividing the GPe into four subregions along the dorsoventral and lateromedial axes (Fig. 1c). We selectively expressed tdTomato in iMSNs by crossing Adora2A-Cre mice with Ai9 mice to visualize striatopallidal axon fibers. We quantified

both striatopallidal and dopaminergic axonal areas in the GPe through double-immunostaining for tyrosine hydroxylase (TH) and tdTomato (RFP). The regional expression of tdTomato in Adora2A-Cre;Ai9 mice was consistent across the different subregions of the GPe (Fig. 1d). Interestingly, although TH-positive DA fibers are comparable within the striatal regions[21], TH-positive DA axons innervated the GPe with significant spatial heterogeneity; DA fibers are more abundant in the medial and ventral parts of the GPe compared to the lateral and dorsal regions (Fig. 1e,f). To determine whether this anatomical heterogeneity translates into functional differences in DA transmission, we measured stimulus-evoked DA release across GPe subregions using $GRAB_{DA}$ imaging and FSCV. Both approaches detected reliable DA signals throughout the GPe, although regional variation was not clearly observed (Fig. 1g-i and Supplementary Fig. 2d-f).

DA D2-like receptors modulate striatopallidal transmission through distinct mechanisms within the subregions of the GPe

The bath application of either DA or D2-like receptors agonist quinpirole in the GPe has been documented to reduce GABAergic transmission at striatopallidal synapses while simultaneously increasing the paired pulse ratio (PPR)[10,22,23]. These findings indicate a presynaptic action of DA through D2Rs at striatopallidal axon terminals originating from iMSNs. We first revisited the functional role of striatopallidal presynaptic D2Rs on GABAergic synaptic transmission by measuring the PPR to indirectly monitor release probability[24,25]. Most of the previous studies examining striatopallidal synapses have utilized electrical stimulation to evoke striatopallidal synaptic transmission. However, this approach is inherently prone to the unintended activation of other axons including collaterals from dMSNs axons, pallidostriatal axons, and GPe collateral axons[26–28]. To avoid this possibility, we employed optogenetic techniques to selectively stimulate striatopallidal axons[26,27]. Specifically, we expressed channelrhodopsin-2 (ChR2) in iMSNs by crossing Adora2A-Cre mice with transgenic mice harboring a conditional floxed allele of ChR2 in the Rosa26 locus (Ai32 mice) (Fig. 2a). First, we validated the stable maintenance of oIPSC (optically evoked inhibitory postsynaptic current) baselines over a 40-minute period and reliably observed paired-pulse responses at a 50 ms inter-stimulus interval under our recording conditions, in agreement with previous studies using comparable protocols[29–31] (Supplementary Fig. 3a,b). Consistent with previous reports using electrical stimulation[22,23], the application of quinpirole

significantly reduced the light-evoked GABAergic transmission (oIPSCs) and increased the PPR at striatopallidal synapses (Fig. 2b,c and Supplementary Fig. 3c,d). Although differences in the oIPSC kinetics of striatopallidal synaptic transmission were observed depending on the postsynaptic GPe neuronal types (Table S1), the response to DA D2-like receptor activation did not differ between GPe neuronal types, consistent with previous studies[22].

As mentioned above, most prior studies have assumed that striatopallidal synapses in the GPe possess homogeneous physiological characteristics. Given the observed heterogeneity in dopaminergic innervation across the GPe (Fig. 1c-f), we next investigated whether D2-like receptors modulate striatopallidal synaptic transmission in a region-dependent manner. To this end, we divided the GPe into four quadrants along the dorsoventral and mediolateral axes, guided by the distribution pattern of TH-positive fibers, providing an operational framework for subregional analysis (Fig. 2e-h). To minimize ambiguity arising from anatomical boundaries, we avoided recording neurons near quadrant overlaps. Most importantly, we observed that the effect of quinpirole at striatopallidal synapses exhibited significant variation dependent on the specific subregions of the GPe. While quinpirole universally suppressed GABAergic transmission across all subregions of the GPe, it induced distinct alterations in the PPR. Quinpirole treatment increased the PPR in the dorsolateral (DL) and ventromedial (VM) subregions, whereas no significant change in PPR was observed in the ventrolateral (VL) and dorsomedial (DM) subregions of the GPe (Fig. 2e-h and Supplementary Fig. 3e-h). When directly comparing these subgroup pairs, the quinpirole-induced PPR increase was significantly greater in the DL and VM GPe than in the VL and DM GPe, suggesting region-specific modulation within the GPe (Fig. 2d). To further confirm both the robustness and the reversibility of this subregional pattern, we performed additional experiments using a lower concentration of quinpirole (20 nM). As with the 10 μM condition, quinpirole increased the PPR in the DL and VM but not in the VL and DM. Notably, both oIPSC amplitude and PPR fully recovered to baseline after wash-out (Supplementary Fig. 4,5), indicating that the observed modulation represents a reversible D2R-mediated effect rather than a time-dependent rundown. Consistent results were also obtained in adult mice using 20 nM DA application, confirming the reproducibility of this subregional pattern (Supplementary Fig. 6).

In light of the regional heterogeneity observed in dopaminergic modulation within the GPe, we hypothesized the presence of an underlying anatomical factor that might partially account

for this variation. To explore this, we quantified the nearest neighbor distances between putatively functional DA boutons and striatopallidal synapses. Utilizing Adora2A-Cre;Ai9 mice, we performed multi-color immunostaining coupled with enhanced confocal microscopy. The co-localization of the presynaptic protein Bassoon and TH was considered as functional DA boutons[32,33]. Furthermore, striatopallidal GABAergic synapses were identified by the co-localization of presynaptic RFP and postsynaptic $GABA_AR$ (Supplementary Fig. 7a,b). Interestingly, the DL and VM regions of the GPe, which exhibited elevated PPR in response to quinpirole, displayed shorter nearest neighbor distances between functional DA boutons and striatopallidal GABAergic synapses compared to the VL and DM GPe (Supplementary Fig. 7c-g). This anatomical characteristics within the GPe may also have functional implications for the region-dependent variability in dopaminergic modulation of striatopallidal transmission.

Region-specific dopaminergic modulation of striatopallidal synaptic transmission in the GPe is driven by differential contributions of presynaptic D2Rs and postsynaptic D4Rs

To determine how the activation of D2-like receptors differently modulates striatopallidal transmission across various subregions of the GPe, we compared the quantal properties of striatopallidal GABAergic transmission before and after treatment with quinpirole[34,35]. For quantal analysis, Ca^{2+} was substituted with Sr^{2+} in the bath solution to facilitate asynchronous release. Striatopallidal GABAergic transmission in some GPe neurons did not respond to Sr^{2+} treatment; consequently, these cells were excluded from the quantal analysis. It is noteworthy that neurons in the lateral GPe regions (DL, VL) exhibited a lower propensity for evoking asynchronous release. When Sr^{2+} was applied, no significant differences were observed in the quantal amplitude and frequency of oIPSCs among the GPe subregions. Following quinpirole treatment with Sr^{2+} replacement, a reduction in quantal amplitude was observed across all GPe subregions (Fig. 3a-d). However, a decrease in quantal frequency was specifically found in the DL and VM GPe subregions (Fig. 3a,d,e), where an elevation in PPR by quinpirole was also detected. Direct subgroup comparison further showed that the reduction in quantal frequency was significantly greater in the DL and VM GPe than in the VL and DM GPe (Fig. 3f). These findings suggest that the activation of postsynaptic D2-like receptors in the GPe universally suppresses GABAergic transmission across all subregions, while presynaptic D2-like receptors in the DL and VM GPe

modulate GABA release.

To explore potential regional variations in the quantal kinetics of striatopallidal synaptic transmission in the GPe, we conducted a clustering analysis on Sr^{2+}-induced quantal responses. This analysis aimed to determine whether specific quantal characteristics varied across the DL, VL, DM, and VM regions of the GPe. Each quantal response was characterized by amplitude, rise time, and decay constant, standardized across cells, and subjected directly to a recursive k-means clustering procedure. This analysis yielded 27 stable clusters across all responses (Supplementary Fig. 8a). Comparison of these categories across the GPe subregions revealed a notable divergence in the VM region. Unlike the DL, VL, and DM regions, which shared similar quantal characteristics, the VM region exhibited unique quantal categories with significantly different kinetics (Supplementary Fig. 8b-e and Table S2). This distinct pattern may indicate that striatopallidal synapses in the VM region of the GPe may originate from functionally different sources in the striatum or employ a unique set of presynaptic mechanisms, potentially reflecting functional specialization within the GPe circuitry. As a further investigation into the synaptic vesicle release machinery, we examined the individual isoforms of synaptotagmin at striatopallidal axon terminals to determine potential subregional variations in the presynaptic fusion machinery within the GPe (Supplementary Fig. 9a,d,g). Our findings showed that striatopallidal terminals are predominantly co-localized with synaptotagmin 1 across all GPe subregions (Supplementary Fig. 9j,k). Synaptotagmin 7 exhibited slightly higher expression in the medial and dorsal regions relative to the lateral and ventral regions of the GPe (Supplementary Fig. 9e,f), while synaptotagmin 5/9 was preferentially localized in the dorsal GPe compared to the ventral GPe (Supplementary Fig. 9h,i). These observations implicate subregion-specific heterogeneity of striatopallidal synapses in basal synaptic features including quantal characteristics and synaptic release machinery. While these differences in quantal kinetics and synaptotagmin expression do not directly explain the observed DA modulation, they support the notion that striatopallidal synapses exhibit subregion-specific molecular and physiological heterogeneity.

We next focused on identifying D2-like receptors at presynaptic and postsynaptic sites of striatopallidal synapses across the different GPe subregions. GPe neurons in rodents are reported to express DA D4 receptors (D4Rs)[11,12], yet there are conflicting studies regarding the postsynaptic dopaminergic effects on striatopallidal synaptic transmission[13,22,23]. We pharmacologically

evaluated the postsynaptic effect of D4Rs on striatopallidal transmission using optogenetic stimulation combined with a highly selective D4R agonist A-412997 (2-(3′,4′,5′,6′-tetrahydro-2′H-[2,4′] bipyridinyl-1′-yl)-N-m-tolyl-acetamide). If GABAergic transmission at striatopallidal synapses is suppressed by postsynaptic D4Rs, treatment with a selective D4R agonist A-412997 would result in an attenuation of oIPSCs without altering the PPR. Consistent with our quantal analysis of striatopallidal transmission, treatment with A-412997 led to a widespread reduction in oIPSCs across all GPe subregions, without affecting the PPR (Supplementary Fig. 10 and Supplementary Fig. 11c-f). This finding suggests that postsynaptic D4Rs inhibit GABAergic transmission uniformly throughout the GPe. To clearly validate the region-specific role of presynaptic D2Rs in regulating GABA release at striatopallidal synapses, we assessed the effects of quinpirole on oIPSCs and PPR under continuous bath application of the D2R-selective antagonist L-741626. We found that quinpirole continued to decrease GABAergic transmission in the presence of L-741626 application; however, the previously observed increase in PPR induced by quinpirole was no longer present in the DL and VM GPe regions (Fig. 3g-j and Supplementary Fig. 11a,b). These two complementary pharmacological approaches together indicate that postsynaptic inhibition is uniformly mediated by D4Rs, whereas regionally distinct presynaptic modulation is driven by presynaptic D2Rs.

We next questioned whether differences in the localization and spatial distribution of D2Rs at striatopallidal axon terminals might contribute, at least in part, to the region-specific dopaminergic modulation of synaptic transmission in the GPe. To selectively label striatopallidal axons and synaptic terminals, we injected a Cre-inducible adeno-associated virus (AAV) expressing both mGFP and synaptophysin-mRuby into the entire striatum of Adora2A-Cre mice (Fig. 4a,b). Subsequently, we performed multi-color immunostaining and enhanced confocal imaging to quantify the spatial localization of D2Rs at striatopallidal axon terminals (RFP+) or axons (GFP+) within each GPe subregion (Fig. 4c). Our results revealed that the DL and VM GPe subregions exhibited a higher degree of co-localization of D2Rs on striatopallidal axons (D2R+ GFP+) and axon terminals (D2R+ RFP+) compared to the VL and DM GPe subregions (Fig. 4d and Supplementary Fig. 12a). Additionally, the nearest neighbor distance between D2Rs on striatopallidal axons or axon terminals was shorter in the DL and VM GPe compared to the VL and DM GPe (Fig. 4e). We also investigated the expression of D4Rs and $GABA_A$Rs on

postsynaptic neurons in the GPe. In Adora2A-Cre;Ai9 mice, striatopallidal axons were labeled with RFP and $GABA_AR$s were immunostained to mark the dendrites of GPe neurons (Fig. 4f,g). Using multi-color immunostaining and 3D reconstruction, we were able to clearly identify the separation between striatopallidal axons (RFP+) and postsynaptic neuronal dendrites labeled with $GABA_AR$ in the GPe (Fig. 4h). We found that both the volume and number of D4R-positive signals were significantly greater in the VL and DM GPe subregions compared to the DL and VM GPe, whereas no significant differences were observed in the volume and number of $GABA_AR$-positive signals (Fig. 4i,j and Supplementary Fig. 12b,c). Furthermore, the nearest neighbor distances between D4Rs and $GABA_AR$s were markedly shorter in the VL and DM GPe compared to the DL and VM GPe (Fig. 4k). These findings suggest that region-specific differences in the expression, localization, and spatial distribution of presynaptic D2Rs and postsynaptic D4Rs may partially underly the distinct dopaminergic modulation of striatopallidal transmission observed across GPe subregions.

Pre- and postsynaptic DA receptors fine-tune ongoing activity in the GPe through region-specific modulations

Information spanning a wide range of frequencies, from low to high, propagates through the basal ganglia circuits including the indirect pathway. To further explore the functional implications of region-specific dopaminergic modulations on striatopallidal transmission, beyond their effects on PPR, we investigated how DA receptor activation influences ongoing activity at striatopallidal synapses. We optogenetically stimulated striatopallidal axon terminals with trains of 10 light pulses at 20 Hz, and compared the inhibitory postsynaptic responses across the GPe subregions[29]. We found that postsynaptic responses to 10-pulse stimulation varied significantly depending on the anatomical location within the GPe (Fig. 5a,d,g,j). High-frequency stimulation often leads to short-term depression at synapses, primarily due to the depletion of the readily releasable pool (RRP)[36]. In the GPe, such stimulation induced pronounced short-term depression in the DL and VL subregions, with GABAergic transmission significantly suppressed throughout the stimulation trains (Fig. 5a-f). In contrast, in the VM GPe, oIPSCs were initially facilitated but ultimately transitioned to synaptic depression (Fig. 5j-l). Notably, striatopallidal synapses in the DM GPe consistently exhibited short-term facilitation, underscoring the heterogeneity of synaptic

modulation across GPe subregions (Fig. 5g-i,m).

Upon application of quinpirole at striatopallidal synapses, GABAergic transmission during 10-pulse stimulation was significantly inhibited by DA receptor activation in the DL and VM GPe. However, presynaptic mechanisms partially counteracted this inhibition, sustaining short-term facilitation to mitigate frequency-dependent suppression (Fig. 5b,c,k,l,n). In contrast, oIPSCs were consistently suppressed by high-frequency stimulation in the VL GPe, where GABAergic transmission had previously been diminished by quinpirole without any change in the PPR. To assess the difference between the initial and final responses elicited by the 20 Hz stimulation, the ratio of the oIPSC amplitude for the tenth stimulus (P10) to that of the first stimulus (P1) was calculated. The lack of change in the P10/P1 ratio following quinpirole treatment suggests that DA receptor activation in the VL GPe affects striatopallidal transmission exclusively through gain modulation (Fig. 5e,f). Similarly, in the dorsomedial (DM) GPe, quinpirole attenuated GABAergic transmission, and the P10/P1 ratio remained unchanged, further indicating gain modulation. Despite this, striatopallidal synapses in the DM GPe sustained synaptic transmission by maintaining short-term facilitation, thereby functioning as a high-pass filter independent of DA receptor activation (Fig. 5h,i). Additionally, the charge ratio, which quantifies the relative suppression of trains of oIPSCs normalized to the suppression of single oIPSC[29], differed between the DL-VM GPe and VL-DM GPe (Fig. 5n). These findings collectively suggest that ongoing activity at striatopallidal synapses is differentially shaped based on the anatomical location within the GPe. Moreover, while GABAergic transmission at striatopallidal synapses is universally suppressed by DA receptor activation throughout the GPe, pre- and postsynaptic DA receptors fine-tune this transmission in a region-specific manner.

Dopaminergic axons are differentially denervated by 6-OHDA across the GPe subregions

Given that the dopaminergic projections from the SNc primarily follow the nigrostriatal pathway, which predominantly innervates the striatum, the degeneration of TH-positive dopaminergic axons, a key pathological hallmark of Parkinson's disease (PD), has been extensively characterized within the striatum. However, several studies have also reported pathological alterations in dopaminergic innervation of the GPe in both human patients and animal models[37–39]. This led us to investigate whether the degeneration of dopaminergic axons in animal models of DA depletion exhibits

regional heterogeneity within the GPe. To investigate whether dopaminergic axons in the GPe are themselves heterogeneous across subregions, and whether such heterogeneity might provide a cellular and anatomical basis for region-specific dopaminergic modulation, we examined the spatiotemporal pattern of axonal degeneration following DA depletion. To induce DA depletion pharmacologically, we unilaterally infused 6-hydroxydopamine (6-OHDA) into the medial forebrain bundle (MFB) of Adora2A-Cre;Ai9 mice (Supplementary Fig. 13a). We then examined the time-dependent denervation of DA axons in the GPe subregions at 1, 3, and 5 days post-6-OHDA administration using double immunostaining for TH and RFP (Supplementary Fig. 13b). Because this model does not fully recapitulate the progressive pathology of Parkinson's disease, we hereafter refer to it as a DA depletion model. Under these conditions, DA axons were significantly diminished in the DLS, the primary projection target of SNc DA neurons, as early as one day after the 6-OHDA injection (Supplementary Fig. 13c,f,g). As depicted in Figure 1, the heterogeneity in DA axonal innervation across GPe subregions was also preserved in the contralateral hemisphere, and TH-positive axonal loss relative to the contralateral side varied across GPe subregions and time points (Supplementary Fig. 13d,e). Notably, the degeneration of DA axons in the DL, VL, and VM regions of the GPe, similar to the DLS, was observed as early as one day post-6-OHDA injection. In contrast, DA axons in the DM GPe remained relatively intact at Day 1, whereas the DL GPe showed the mildest reduction at Day 5 (Supplementary Fig. 13d,e). Collectively, these findings suggest that DA axons in distinct GPe subregions display differential temporal susceptibility to degeneration following DA depletion.

DA depletion reorganizes region-specific dopaminergic modulation of striatopallidal synaptic transmission

Studies in both nonhuman primates and humans have demonstrated increased oscillatory synchronization in the GPe of Parkinsonian models and PD patients[40,41]. In addition, several studies in rodent models suggest that the heightened striatopallidal GABAergic inhibition of the GPe under DA-depleted conditions may contribute to the pathophysiological changes observed in the GPe[10,42]. We sought to determine whether dopaminergic modulation of striatopallidal transmission in the GPe is also altered in a region-specific manner under DA-depleted conditions. To unravel the physiological changes in striatopallidal transmission under DA-depleted conditions,

we unilaterally injected 6-OHDA into the MFB of Adora2A-Cre;Ai32 mice (Fig. 6a). To capture early-stage synaptic adaptations to DA loss, we conducted electrophysiological recordings at 3 days post-6-OHDA infusion. Three days post-6-OHDA infusion, we bath-applied quinpirole and measured oIPSCs and PPR changes across different GPe subregions (Fig. 6b-e). In the contralateral hemispheres, we replicated the region-specific dopaminergic modulation of striatopallidal synaptic transmission; oIPSCs decreased with an increased PPR in the DL and VM GPe, whereas oIPSCs were reduced without a change in PPR in the VL and DM GPe (Supplementary Fig. 14,15).

Upon quinpirole treatment, the accompanying changes in PPR exhibited a subregion-specific reorganization under DA-depleted conditions. To provide complementary perspectives, we analyzed both absolute PPR values and normalized changes relative to baseline. In the absolute PPR values, DA depletion reduced baseline PPR selectively in the VL GPe, consistent with previous reports showing decreased PPR following DA depletion[43], and produced a robust quinpirole-induced increase in the DM GPe (Supplementary Fig. 14b,c,e). These absolute measures reflect basal differences in short-term plasticity (STP) and the absolute expression of drug-induced changes. In contrast, normalized analyses, which highlight relative modulation capacity rather than absolute baseline differences, revealed that DA depletion abolished the quinpirole-induced facilitation of PPR in the DL GPe (Fig. 6b,f,g). In the VM GPe, facilitation was still detectable but significantly attenuated compared to the contralateral side (Fig. 6e,f,g). Conversely, in the VL and DM GPe, where PPR was largely unchanged by quinpirole under normal conditions, DA depletion led to the emergence of a robust facilitation (Fig. 6c,d,f,g). Together, these findings suggest that dopaminergic modulation of striatopallidal STP is differentially affected by DA depletion in the DL-VM and VL-DM subregions of the GPe.

DA depletion induces region-specific alterations in the spatial distribution of presynaptic D2Rs at striatopallidal axon terminals

In light of the possibility that variations in the spatial distribution and localization of D2Rs at striatopallidal axon terminals may contribute to region-specific dopaminergic modulation of striatopallidal transmission within the GPe, we further investigated whether DA depletion induces region-specific alterations in the spatial distribution and localization of D2Rs. Striatopallidal axons

and axon terminals were labeled with GFP and RFP (mRuby), respectively, by injecting AAVs into the entire striatum (Fig. 7a). Following 6-OHDA injection, we performed multi-color immunostaining and utilized enhanced confocal imaging with airyscan in each subregion of the GPe (Fig. 7b and Supplementary Fig. 12d,e). We replicated our findings from Figure 4, demonstrating that D2Rs were more localized in the striatopallidal axons and axon terminals within the DL and VM GPe compared to the VL and DM GPe in the contralateral hemisphere (Fig. 7c). To further delve into the spatial relationship between presynaptic D2Rs and striatopallidal axon terminals in each subregion of the GPe, we conducted clustering analysis using Ripley's H function, which is particularly sensitive to spatial point patterns[44,45]. When the nearest distances from striatopallidal axon terminals (RFP+) to D2Rs in the VL and DM subregions of the GPe were used as a null model, clustering analysis revealed that the DL and VM GPe exhibited a greater tendency for clustered features between striatopallidal axon terminals and D2Rs (Fig. 7e). The results were reversed when the null model was replaced by the nearest distances from striatopallidal axon terminals to D2Rs in the DL and VM GPe, indicating that striatopallidal axon terminals and D2Rs appeared to be less clustered in the VL and DM GPe (Fig. 7e).

However, following DA depletion induced by 6-OHDA infusion, the differences in D2R localization at striatopallidal axons and axon terminals between the DL-VM and VL-DM subregions of the ipsilateral GPe were no longer observed (Fig. 7d). Under this DA-depleted condition, the difference in the level of clustering between striatopallidal axon terminals and D2Rs also became less pronounced between the DL-VM and VL-DM subregions of the GPe (Fig. 7f). Interestingly, following DA depletion, the expression of D2Rs on striatopallidal axon terminals increased significantly in the VL and DM GPe subregions (Fig. 7g). Moreover, the post-DA depletion led to a marked enhancement in the clustering of striatopallidal axon terminals and D2Rs in the ipsilateral GPe, in contrast to the contralateral GPe. This finding was further supported by rejection rates exceeding 70%, calculated as the proportion of samples for which the null model was rejected using the Diggle-Cressie-Loosmore-Ford (DCLF) test[46] (Fig. 7h).

Under the same experimental conditions (Supplementary Fig. 16a), we also examined the spatial relationship between dopaminergic boutons and striatopallidal axon terminals after DA depletion. The co-localization of TH and vesicular monoamine transporter 2 (VMAT2) immunofluorescence was considered indicative of potential dopaminergic boutons, while RFP

(mRuby)-positive fluorescence was used to identify putative striatopallidal axon terminals (Supplementary Fig. 16b,c). We found no changes in the area of striatopallidal axons (GFP+) or axon terminals (RFP+) within the GPe following DA depletion (Supplementary Fig. 16d,e). Notably, in the contralateral hemisphere, more contact areas between dopaminergic boutons and striatopallidal axon terminals (or axons) were observed in the DL and VM GPe compared to the VL and DM GPe. This regional difference, however, was absent in the 6-OHDA-lesioned ipsilateral hemisphere (Supplementary Fig. 16f). In the ipsilateral hemisphere, the areas of both dopaminergic axons and boutons were significantly reduced across all GPe subregions (Supplementary Fig. 16g). Furthermore, no significant differences in the nearest neighbor distances between dopaminergic boutons and striatopallidal axon terminals were observed among the GPe subregions, nor were there significant changes in the spatial relationship between striatopallidal axon terminals (Supplementary Fig. 16h,i). Taken together, our findings reveal that denervation of dopaminergic axons and DA depletion can lead to region-specific alterations in the expression, localization, and spatial distribution of D2Rs on striatopallidal axon terminals within the GPe. These changes may contribute to the functional modifications observed in the dopaminergic modulation of striatopallidal transmission.

DA depletion may lead to region-specific changes in calcium dynamics at striatopallidal synapses

To further investigate the physiological mechanisms underlying the heterogeneous dopaminergic modulation of striatopallidal STP under both control and DA-depleted conditions, we utilized a computational modeling approach based on the Tsodyks-Markram model, which describes the dynamics of STP under general conditions[47,48] (Fig. 8a). To define the parameter search space for model optimization, we set lower and upper bounds for each parameter (Table S3). Consistent with our quantal analysis (Fig. 3a-f), the computational model successfully reproduced the experimentally observed subregion-specific patterns of dopaminergic modulation by incorporating the calcium channel open probability as a key variable modulated by quinpirole[49,50] (Fig. 8b). Importantly, this computational model was deliberately constrained to presynaptic calcium dynamics rather than incorporating the full GPe circuitry, thereby enabling direct validation with axon terminal calcium imaging and PPR measurements. Under control conditions, the

computational model predicted a selective decrease in calcium channel open probability and intracellular calcium concentration within the striatopallidal axon terminals of the DL and VM GPe subregions (Fig. 8c-f). In contrast, under DA-depleted conditions, the model indicated a marked reduction in calcium channel open probability and calcium concentration across all GPe subregions, except for the DL GPe (Fig. 8g-j).

To directly assess presynaptic Ca^{2+} dynamics, we performed axon terminal calcium imaging across GPe subregions (Supplementary Fig. 17). To selectively label striatopallidal axon fibers, we injected an AAV expressing GCaMP6f into the whole striatum of Adora2A-Cre mice. Fluorescence signals were recorded from bouton-like structures, and Ca^{2+} transients were compared before and after quinpirole application in both control and DA-depleted conditions. Under control conditions, quinpirole significantly reduced Ca^{2+} transients in the DL and VM GPe subregions, whereas responses in the VL and DM GPe subregions were largely unchanged, showing clear regional differences between GPe subgroups (Supplementary Fig. 17c,d). In contrast, following DA depletion, quinpirole-induced suppression of Ca^{2+} signals was diminished in the DL GPe, partially retained in the VM GPe, and newly observed in the VL and DM GPe, eliminating the subgroup differences present under control conditions (Supplementary Fig. 17c,e).

To further validate the modeling framework, we compared the simulated outputs with the experimental values of PPR and Ca^{2+} responses (Supplementary Fig. 18). The simulated and experimental PPR values and Ca^{2+} responses were closely matched across subregions and conditions, capturing the overall direction and variability of dopaminergic modulation (Supplementary Fig. 18a,b). Representative overlays of experimental and simulated IPSCs further revealed general correspondence in paired-pulse dynamics and temporal features (Supplementary Fig. 18c). To provide a quantitative assessment of model performance, we computed the mean squared error (MSE) and root mean squared error (RMSE) between simulated and experimental values for each condition (Table S4). Overall, the model reproduced experimental PPR changes and Ca^{2+} responses across subregions, although RMSE values were notably higher under 6-OHDA conditions, indicating greater complexity of IPSC dynamics in the DA-depleted state[51,52]. Together, these results suggest that DA depletion drives distinct synaptic adaptations at striatopallidal synapses depending on their spatial locations within the GPe, further highlighting the region-specific mechanisms that govern synaptic transmission in this nucleus.

Discussion

We demonstrate here that information transmitted via the indirect pathway can be modulated through presynaptic D2Rs and postsynaptic D4Rs in a subregion-specific manner within the GPe. DA depletion exerts differential and region-specific effects on the presynaptic modulation of GABA release mediated by D2Rs. The GPe, previously considered a simple relay station in the indirect pathway, possesses a heterogeneous neuronal composition with distinct characteristics and functions[53–56]. These findings unveil a previously unrecognized role of dopaminergic modulation in the GPe, highlighting its complex, anatomically specific effects on striatopallidal synaptic transmission.

The distinct DA modulation of striatopallidal transmission within the GPe subregions through D2-like DA receptors was topographically organized in a pinwheel-like fashion along two orthogonal, diagonal axes: the DL-VM and VL-DM orientation. This anatomical organization is particularly intriguing when considered alongside a recent work demonstrating that GPe projections to the subthalamic nucleus (STN) are also topographically aligned linearly along two diagonal gradient axes[57]. Given the parallel connectivity of the indirect pathway within the cortex-basal ganglia-thalamic network[14] the topographic alignment of dopaminergic modulation in the GPe subregions may play a critical role in shaping information processing in the downstream nuclei of the basal ganglia circuitry.

In addition to such spatial topography, the GPe is composed of heterogeneous neuronal subtypes with distinct molecular markers, intrinsic properties, and projection targets. Classic studies have distinguished prototypic and arkypallidal neurons[53,58,59], and subsequent work has demonstrated that manipulating specific subtypes can differentially influence motor function in Parkinsonian mice[56,60,61]. Further electrophysiological and in vivo analyses have revealed additional functional diversity, including differences in firing patterns, input specificity, and sensory responsiveness across subtypes[62–65]. While our study did not reveal subtype-dependent differences in D2R-mediated modulation of striatopallidal transmission, the pinwheel-like spatial organization we describe may represent a mesoscale framework within which such molecular markers and functionally distinct GPe populations are embedded. Integrating spatial topology with cell-type identity will be an important direction for future studies aimed at understanding how

heterogeneity at both levels shapes information flow through the indirect pathway.

Monitoring DA with FSCV has been challenging due to the limited sensitivity of electrochemical techniques. The fluorescent DA sensor $GRAB_{DA}$, allowed for direct monitoring of DA release from dopaminergic terminals within the GPe. We took advantage of optogenetic stimulation to selectively drive striatopallidal transmission. The most intriguing finding in our investigation of striatopallidal transmission is that, while the D2-like DA receptor agonist quinpirole ubiquitously attenuated GABAergic transmission at striatopallidal synapses, it increased the PPR only in the DL and VM GPe. In contrast, the PPR remained unaffected in the VL and DM regions of the GPe. By analyzing the effects of quinpirole on quantal properties of striatopallidal transmission across the GPe subregions and employing D2R- and D4R-selective antagonists, we discovered that postsynaptic D4Rs at striatopallidal synapses mediate the suppression of GABAergic transmission irrespective of the anatomical locations within the GPe. However, presynaptic D2Rs effectively inhibited presynaptic GABA release exclusively in the DL and VM GPe. Regional differences in the expression, localization, and spatial distribution of presynaptic D2Rs and postsynaptic D4Rs at striatopallidal synapses may contribute to the distinct dopaminergic modulation we observed across GPe subregions. Notably, D4Rs are known to suppress GABAergic currents via postsynaptic, PKA-dependent signaling cascades[13,66], which may underlie the D4R-mediated modulation observed in our study. The efficacy of presynaptic D2R activation and its signal transduction may also vary depending on the alternatively spliced isoforms of D2Rs expressed on striatopallidal axon terminals in each subregion of the GPe[67,68]. Moreover, presynaptic modulation of total calcium influx via D2Rs may exhibit significant divergence across the GPe subregions.

Various STP regulation modes have been identified across several brain regions, including the cortex[69], cerebellum[70], and hippocampus[71]. In addition, both canonical and noncanonical presynaptic modulation can coexist at the same synapses in the prefrontal cortex[29], suggesting the presence of diverse mechanisms for precisely and finely tuning synaptic functions. Striatopallidal synapses, serving as the initial gateway of the indirect pathway, represent a critical node that can profoundly influence the overall output of this pathway. Synaptic DA modulation may become even more diverse when ongoing synaptic activity is propagated through the striatopallidal synapses. When stimulated with trains of light pulses, the entire sequence of oIPSCs progressively

depressed in the lateral GPe, including the DL and VL regions. Moreover, stimulation of D2-like receptors with quinpirole led to an additional suppression of striatopallidal transmission in the DL and VL GPe. However, STP at striatopallidal synapses in the DL GPe allowed ongoing activity to be sustained toward the end of the stimulation. In contrast, synaptic activities in the VL GPe were continuously suppressed, with the last oIPSC showing the strongest attenuation.

In the case of medial GPe, including the DM and VM regions, continuing activity facilitated synaptic transmission at striatopallidal synapses. This facilitation was observed throughout the entire sequence of all ten oIPSCs in the DM GPe or at least during the first half of the synaptic transmission in the VM GPe. Although the activation of D2-like receptors in the medial GPe universally attenuated GABAergic transmission, as observed in the lateral GPe, a high-pass filtering mechanism consistently promoted synaptic transmission in the DM GPe. Notably, this facilitation occurred independently of D2-like receptor activation. Neurons in the GPe also receive excitatory inputs directly from the STN and indirectly from the cortex. Thus, the facilitating nature of striatopallidal transmission in the DM GPe likely acts as a high-pass filter, preferentially transmitting strong or repetitive inhibitory bursts while attenuating weaker inputs[72–74]. This property may shape how DM GPe neurons integrate convergent synaptic activity, independent of their intrinsic spontaneous firing.

Our findings collectively suggest that ongoing synaptic information transmitted through striatopallidal synapses is differently shaped along the lateral-to-medial axis of the GPe. Simultaneously, presynaptic mechanisms mediated by D2Rs sustain continuing synaptic activity, particularly in the DL and VM regions of the GPe. It is important to note that although high-frequency, ongoing synaptic activity was gain-modulated without STP in both the VL and DM regions of the GPe, the effects of this modulation differed. In the VL GPe, the synaptic gain was modulated to primarily inhibit striatopallidal transmission, whereas gain modulation functioned to augment synaptic transmission in the DM regions of the GPe. In light of the recent studies revealing topographically graded organization in the basal ganglia circuit[14,57], it is very likely that diverse modalities of information, including sensory, motor, associative, and limbic inputs, may propagate in parallel through the basal ganglia network. Supporting this, diffusion tensor imaging (DTI) studies in human subjects have shown the existence of three parallel channels originating from association, motor, and limbic cortices, which project to distinct striatal regions[75]. Building

on these findings, our study provides insights into how distinct cortical information may be differentially processed and shaped within anatomically parallel subnetworks of the basal ganglia, particularly through the indirect pathway.

A comprehensive understanding of the anatomical organization and functional features of dopaminergic modulation within the basal ganglia circuitry, including striatopallidal synapses in the GPe, is essential for elucidating the pathophysiology of DA-related brain disorders. We found that dopaminergic axons innervating the GPe exhibit region-specific and temporally distinct vulnerabilities to DA depletion. Given the heterogeneous molecular characteristics of DA neurons in the midbrain, this differential vulnerability may stem from their distinct origins within specific DA neuronal subtypes[76–78]. In 6-OHDA-lesioned mice, striatopallidal synapses in the VL and DM subregions of the GPe, where GABAergic transmission was initially suppressed by the activation of D2-like receptors without changes in the PPR, exhibited a significant elevation in PPR following treatment with quinpirole. However, these alterations in PPR observed in the VL and DM GPe may arise from distinct mechanisms. Considering the observed decrease in baseline PPR after DA depletion and the absence of a significant difference in absolute PPR values between ipsilateral and contralateral hemispheres following quinpirole application, it is likely that the enhanced PPR in the VL GPe is due to altered presynaptic release probability resulting from DA depletion[79]. In the case of striatopallidal transmission in the DM GPe under DA-depleted conditions, the PPR in the ipsilateral GPe showed a marked increase following quinpirole application despite no baseline PPR differences between hemispheres. This result potentially indicates either D2R upregulation or increased D2R supersensitivity due to DA depletion[78,80,81]. Furthermore, the enhanced STP at striatopallidal synapses in the DM GPe, induced by D2-like receptor activation, may raise the activation threshold of GPe neurons. Notably, in contrast to the changes in the VL and DM GPe, the increase in PPR by quinpirole treatment was attenuated after DA depletion in the DL and VM subregions of the GPe. As potential molecular and cellular correlates of these functional changes, our immunohistochemical analyses revealed region-specific alterations in the spatial organization of presynaptic D2Rs following DA depletion. Under control conditions, striatopallidal axon terminals in the DL and VM were positioned in closer proximity to D2Rs than those in the VL and DM, as reflected by higher clustering values. Following DA depletion, this subregion-specific clustering pattern was lost, with VL and DM terminals showing increased D2R expression. These

spatial rearrangements parallel the reversal of quinpirole-induced PPR modulation. Given that nanoscale receptor positioning can influence the efficiency of presynaptic inhibition by shaping the coupling between receptor activation and release machinery, these findings suggest that DA depletion likely reshapes dopaminergic control of striatopallidal transmission in a spatially organized, subregion-specific manner[82–84]. Taken together with the observations in the VL and DM GPe, our results indicate that subregion-specific alterations in the expression, localization, and spatial distribution of D2Rs on striatopallidal axon terminals within the GPe may partially, though not entirely, account for the physiological changes in the DL and VM GPe under DA-depleted conditions.

Expanding on these findings, computational modeling revealed subregion-specific differences in calcium dynamics under DA-depleted conditions. By incorporating calcium channel open probability as a critical variable modulated by quinpirole, the modeling outcomes effectively recapitulated the experimentally observed differences in PPR, reinforcing the validity of our experimental findings across GPe subregions. Notably, only the VM GPe retained quinpirole-induced PPR modulation after DA depletion. In addition, quantal analysis of Sr^{2+}-induced responses revealed that the VM GPe exhibited distinct release properties compared to other subregions, implying that striatopallidal terminals in this region possess unique presynaptic characteristics that differentiate it from other subregions of the GPe.

Our axon-terminal Ca^{2+} imaging directly supports the modeling framework by demonstrating that quinpirole reduces presynaptic Ca^{2+} transients in a subregion-specific manner, consistent with the parameterization of Ca^{2+} channel open probability. The model therefore serves as a focused framework to evaluate whether changes in presynaptic Ca^{2+} entry can explain the experimentally observed modulation of STP. Within this constrained framework, the model recapitulated the overall direction and qualitative features of dopaminergic modulation observed experimentally across GPe subregions, underscoring that D2R-mediated modulation of VGCCs is sufficient to account for the observed STP changes. Although the fits were less precise under DA-depleted conditions, likely due to the increased complexity of IPSC kinetics, the model still captured the essential features of modulation. Therefore, our findings demonstrate that striatopallidal synapses within the GPe exhibit dynamic, region-specific responses to DA depletion, reflecting the functional heterogeneity of GPe subregions. Our results also highlight the spatially

organized and functionally diverse adaptations of GPe subregions in maintaining information processing within the basal ganglia under DA-depleted conditions.

In summary, our findings provide evidence that striatopallidal transmission via the indirect pathway can be differentially modulated by DA receptor activation under both normal and DA-depleted conditions, depending on the anatomical locations of striatopallidal synapses along the dorsoventral and lateromedial axes of the GPe. Our data further suggests that region specific differences in the expression, localization, spatial distribution, and functional properties of presynaptic D2Rs and postsynaptic D4Rs at striatopallidal synapses may underlie the distinct dopaminergic modulation observed across different subregion of the GPe. These results provide insights into the functional role of dopaminergic innervation and its modulation of striatopallidal synapses within the GPe under both physiological and DA-depleted conditions.

Methods

Animals

All experimental procedures were conducted by protocols approved by the Institutional Animal Care and Utilization Committee of the Ulsan National Institute of Science and Technology (UNIST). All mice were maintained in C57BL/6J background. Mice were group-housed under a 12 hr light / dark schedule (lights on from 6 AM to 6 PM) and given *ad libitum* access to food and water. Mice were group-housed (up to 5 mice per cage) and bred under standard pathogen-free housing conditions in the animal facility of UNIST. Experiments included both female and male mice in approximately equal proportions. Immunohistochemistry, FSCV, one-photon DA imaging, and axon terminal Ca^{2+} imaging experiments were performed in adult mice aged 8–15 weeks. Given the health and stability of GPe neurons in acute brain slices, patch-clamp recording experiments were conducted in younger mice aged 3–4 weeks. To verify that the observed region-specific modulation patterns also occur under adult conditions, additional recordings using low-concentration DA (20 nM) were performed in adult mice aged 8-15 weeks, which reproduced the same subregional patterns. To specifically express ChR2 in indirect pathway medium spiny neurons (iMSNs), Adora2A-Cre (B6.FVB(Cg)-Tg(Adora2a-cre)KG139Gsat/Mmucd, MMRRC stock number: 036158-UCD) mice were crossed with Ai32 (B6.Cg-Gt(ROSA)26Sor$^{tm32(CAG-COP4*H134R/EYFP)Hze}$/J, Jackson stock number: 024109) mice, producing Adora2A-Cre;Ai32. These

mice were used for optogenetic stimulation of striatopallidal synaptic terminals in whole-cell patch clamp recording experiments. To visualize striatopallidal pathway (axons and axon terminals), Adora2A-Cre;Ai9 mice were generated by crossing Ai9-tdTomato (B6.Cg-Gt(ROSA)26Sor$^{tm9(CAG-tdTomato)Hze}$/J) mice with Adora2A-Cre mice. These mice were also used in immunohistochemistry experiments. Adora2A-Cre mice were used for immunohistochemistry and fluorescence imaging experiments.

One-photon fluorescence imaging in the GPe in acute brain slices

Adult C57BL/6J mice were anesthetized via intraperitoneal injection of zoletil (60 mg/kg, Virbac Korea) and rompun (15 mg/kg, Bayer Korea) mixture solution (zoletil : rompun : saline = 4 : 1 : 20), and AAVs expressing $GRAB_{DA}$ (AAV9-hSyn-rDA1.2a, 3.28×10^{13} vg/ml, WZ Biosciences) were injected (250 nl per injection site at a rate of 100 nl/min) into the DLS (coordinates used, AP: +1.3 mm from the bregma, ML: ±2.25 mm from the bregma, DV: −2.2 mm from the dura), the GPe (coordinates used, AP: -0.45 mm from the bregma, ML: ±2.6 mm from the bregma, DV: −3.5 mm, -3.9 mm from the dura), and the M1 cortex (coordinates used, AP: +1.54 mm from the bregma, ML: ±1.6 mm from the bregma, DV: −0.8 mm from the dura). Three weeks after virus injection, the mice were deeply anesthetized with isoflurane (Piramal Critical Care), then decapitated and the brains were immediately removed and briefly exposed to ice-chilled artificial cerebrospinal fluid (ACSF) containing 125 mM NaCl, 2.5 mM KCl, 1.25 mM NaH_2PO_4, 25 mM $NaHCO_3$, 1 mM $MgCl_2$, 2mM $CaCl_2$ and 15 mM glucose oxygenated with 95% O_2 and 5% CO_2. Acute brain slices were prepared as 300-μm-thick sagittal sections using a tissue vibratome (Leica, VT 1200S). One-photon imaging was performed using a BX51WI microscope (Olympus) equipped with a 40x/0.8 NA water-immersion objective (Olympus) and a SOLIS-565C high-power LED (Thorlabs). A 565 nm LED was used to excite the rDA1.2a sensor, and fluorescence was collected using a 569–594 nm filter (Chroma). Fluorescence images were further acquired using a scientific complementary metal-oxide-semiconductor (sCMOS) camera (Orca-Flash4.0 V3, Hamamatsu) in conjunction with HCImage Live software (Hamamatsu). For electrical stimulation, a bipolar concentric electrode (CBAPB75, FHC) was positioned on the M1 cortex, GPe, and DLS under fluorescence guidance. Dopamine release was evoked by electrical stimulation (0.2 ms pulse duration, ten pulses), controlled using a DS-3 stimulus isolator (Digitimer, UK). Dopamine release

were imaged at a resolution of 512 x 512 pixels/frame, 10 frames/s, with an exposure time of 10 ms. For image analyses, regions of interest (ROIs) expressing rDA1.2a sensor were manually selected and analyzed using ImageJ software (NIH).

Fast-scan cyclic voltammetry (FSCV)

To quantify and compare the magnitude of DA release across different basal ganglia nuclei, we measured evoked phasic DA transmission using the WINCS Harmoni FSCV system[85,86]. Following high-frequency electrical stimulation (100 Hz), we observed reliable DA release in the GPe and DLS. Extracellular real-time DA release was measured using FSCV with carbon-fiber microelectrodes (7 μm diameter carbon fiber enclosed in glass, with an exposed tip length of 50–100 μm beyond the tapered glass seal) positioned in the GPe and DLS. A triangular waveform was applied to the carbon fiber microelectrode (CFM) with a holding potential of -0.4 V, a switching potential of 1.5 V, a scan rate of 400 V/s, and an acquisition frequency of 10 Hz, obtaining the voltammogram (current-voltage curve). The initial signal detected in FSCV is the background current, which is induced by ions near the CFM, but when DA is actually present, additional oxidative current at +0.6 V and reductive current at -0.2 V are observed. Therefore, by utilizing background subtraction to remove the signal in the absence of DA from the background voltammogram, only the redox current response to DA remains, allowing real-time estimation of DA concentration. To measure DA release induced by stimulation, a bipolar pulse was delivered to each region with the following stimulation parameters: type, bipolar pulse; frequency, 100 Hz; intensity, 300 μA; pulse width, 2 ms; duration, 4 sec (total of 400 pulses). All FSCV measurements and stimulations were simultaneously performed using the WINCS Harmoni device and WINCSware software. Calibration curves were obtained for DA concentrations of 20, 40, 60, 80, 100, 400, 700 and 1000 nM to convert DA oxidation current signals acquired by FSCV into actual concentration values. To generate the calibration curves, linear regression analyses were performed separately within the concentration ranges of 20 to 100 nM and 100 to 1000 nM.

Immunohistochemistry and confocal imaging

Mice were deeply anesthetized by intraperitoneal injection of zoletil (60 mg/kg, Virbac Korea) and rompun (15 mg/kg, Bayer Korea) mixture solution (zoletil : rompun : saline = 4 : 1 : 20) and

perfused transcardially with phosphate buffer (PB), followed by 4% paraformaldehyde (PFA, Sigma-Aldrich). Brains were rapidly removed and postfixed in 4% PFA at 4°C for overnight. Fixed brains were transferred to 30% sucrose in 0.01 M PB for cryoprotection. Brain sections were made into 20 μm thick sagittal slices using frozen section technique (Microtome SM2010, Leica). Obtained free-floating brain sections were washed with PBS, PBST (0.5% Triton X-100) and blocked with PBST containing 10% normal goat serum (NGS, Sigma-Aldrich) and 2% bovine serum albumin (BSA, Sigma-Aldrich). After blocking, brain sections were incubated with an anti-tyrosine hydroxylase antibody (rabbit polyclonal, 1:1000, ab112, Abcam), an anti-tyrosine hydroxylase antibody (chicken polyclonal, 1:500, ab76442, Abcam), an anti-RFP antibody (Guinea pig polyclonal, 1:1000, 390 005, Synaptic Systems), an anti-RFP antibody (mouse monoclonal, 1:1000, MA5-15257, Thermo Fisher Scientific), an anti-GFP antibody (chicken polyclonal, 1:1000, GFP-1010, Aves Labs), an anti-GFP antibody (mouse monoclonal, 1:1000, sc-9996, Santa Cruz Biotechnology), an anti-bassoon antibody (guinea pig polyclonal, 1:500, 147 004, Synaptic Systems), an anti-bassoon antibody (mouse monoclonal, 1:500, ADI-VAM-PS003-D, Enzo Life Sciences), an anti-VMAT2 antibody (rabbit polyclonal, 1:1000, VMAT2-Rb-Af720, Nittobo Medical), an anti-$GABA_AR\alpha1$ antibody (rabbit polyclonal, 1:2000, GABAARa1-Rb-Af660, Nittobo Medical), an anti-synaptotagmin 1 antibody (mouse monoclonal, 1:1000, 105 011, Synaptic Systems), an anti-synaptotagmin 7 antibody (rabbit polyclonal, 1:200, 105 173, Synaptic Systems), an anti-synaptotagmin 5/9 antibody (rabbit polyclonal, 1:500, 105 053, Synaptic Systems), an anti-VGAT antibody (rabbit polyclonal, 1:1000, 131 003, Synaptic Systems), an anti-VGAT antibody (guinea pig polyclonal, 1:1000, 131 004, Synaptic Systems), an anti-Dopamine D2 receptor antibody (rabbit polyclonal, 1:500, AB5084P, Sigma-Aldrich), an anti-Dopamine D4 receptor antibody (rabbit polyclonal, 1:500, PA5-28756, Thermo Fisher Scientific) in blocking solution at 4℃ overnight, followed by secondary antibodies (goat anti-rabbit, goat anti-mouse, goat anti-chicken, goat anti-guinea pig, 1:1000, Invitrogen) conjugated to Alexa 405, Alexa 488, Alexa 594, and Alexa 647 fluorophores in blocking solution at room temperature for 2 hours. After washing with PBST and PBS, brain slices were mounted onto slides using a mounting medium (P36934 or P36935, Invitrogen).

For quantitative analysis, fluorescence images were captured by an FV1000 confocal laser scanning microscope (Olympus) using a 40x/0.95 NA water immersion objective (zoom factor:

1.5, image size: 512 x 512 pixels), an LSM780N multi-photon confocal laser scanning microscope with airyscan (Carl Zeiss) using a 63x/1.46 NA oil immersion objective (zoom factor: 3, image size: 1248 x 1248 pixels), and an LSM880 multi-photon confocal laser scanning microscope with airyscan (Carl Zeiss) using a 63x/1.4 NA oil immersion objective (zoom factor: 3, image size: 5827 x 5827 pixels for stitched images or 1248 x 1248 pixels). Imaging areas were randomly selected and then images were captured from each target region. Images were further analyzed by Zen software (Carl Zeiss), ImageJ program (NIH, measure function), and MATLAB (MathWorks, custom codes). Confocal 3D images were acquired using the z-stack function of LSM880 confocal laser scanning microscope with Airyscan. Images were collected at 0.185 µm intervals and 3.6993 µm depth with a 63x oil-immersion objective, 3x optical zoom, and a resolution of 1248 x 1248 pixels. 3D images were reconstructed and further analyzed by IMARIS 9.6 software.

Brain slice preparation for electrophysiology

Sagittal brain slices containing the GPe and striatum (250 µm thick) were prepared for whole-cell patch clamp recording. Mice were anesthetized with isoflurane (Piramal Critical Care), decapitated, and the brain was briefly exposed to cold ACSF containing 125 mM NaCl, 2.5 mM KCl, 1.25 mM NaH_2PO_4, 25 mM $NaHCO_3$, 1 mM $MgCl_2$, 2mM $CaCl_2$ and 15 mM glucose oxygenated with 95% O_2 and 5% CO_2. Acute brain slices were obtained using a tissue vibratome (Leica, VT 1200S) in ice-cold ACSF. Brain slices were first maintained in ACSF for 20 min at 34°C and then another 30 min at room temperature. For adult mice used in low-dose DA (20 nM) experiments, slices were prepared in N-methyl-D-glucamine (NMDG)–based cutting solution (in mM: 93 NMDG, 2.5 KCl, 1.2 NaH_2PO_4, 30 $NaHCO_3$, 20 HEPES, 25 glucose, 5 Na-ascorbate, 2 Thiourea, 3 Sodium Pyruvate, 12 N-Acetylcysteine, 10 $MgSO_4 \cdot 7H_2O$, and 0.5 $CaCl_2 \cdot 2H_2O$, 300 - 310 mOsm, pH 7.3 with HCl) after transcardially perfused with an ice cold NMDG solution. Brain slices were immediately transferred to 32°C NMDG solution for 10 min, followed by recovery in ACSF at room temperature for 30 min. After recovery, slices were transferred to a submerged recording chamber perfused with ACSF at a rate of 2 – 3 ml/min at 30 – 31°C. Brain slices were used for electrophysiological recordings within 5 hours following slice preparation.

Electrophysiology, optogenetic stimulation, and pharmacology

GPe neurons were visually identified by conventional IR-DIC optics (BX51WI, Olympus). Whole-cell voltage clamp recordings were made with borosilicate glass pipettes (3.5 – 5.5 MΩ) filled with Cs^+ based low Cl^- internal solution containing 135 mM $CsMeSO_3$, 10 mM HEPES, 1 mM EGTA, 3.3 mM QX-314, 0.1 mM $CaCl_2$, 4 mM Mg-ATP, 0.3 mM Na_3-GTP, 8 mM Na_2-phosphocreatine (290 – 300 mOsm, pH 7.3 with CsOH). To measure inhibitory synaptic currents from the GPe neurons, the membrane potential was held at +0 mV (reversal potential of ionotropic glutamate receptors) under the voltage clamp mode with liquid junction potential correction. Access resistance was maintained between 10 – 20 MΩ, and only cells with less than a 20% change in access resistance were included in the analysis. Whole-cell patch clamp recordings were performed using Multiclamp 700B (Molecular Devices) and signals were filtered at 2 kHz and digitized at 10 kHz (NI PCIe-6259, National Instruments). Recording data were monitored and acquired by WinWCP (Strathclyde software, http://spider.science.strath.ac.uk/sipbs/software_ses.htm), further analyzed offline using Clampfit 10.7 software (Molecular Devices) and OriginPro 2017 (OriginLab). To stimulate ChR2-expressing striatopallidal axons, blue laser light (450 nm, 0.2 ms pulses with 40 sec intervals, 50% of saturation power under the objective less than 1 mW) from diode laser (MDL-III-450, Opto Engine LLC) was focused on the back focal plane of the objective to generate wide-field illumination.

To examine the effects of quinpirole, recordings were divided into three epochs: baseline, drug application (ON), and washout (OFF). For standard quinpirole experiments (10 μM), a stable 15-minute baseline was first obtained prior to drug application. Quinpirole was then bath-applied for 10 minutes (quinpirole ON), followed by a 15-minute washout in drug-free ACSF (quinpirole OFF). For low-dose quinpirole experiments (20 nM), a 10-minute baseline was obtained, followed by a 10-minute drug application and a subsequent 15-minute washout. For each condition, data points within the respective time window (baseline, quinpirole ON, quinpirole OFF) were averaged to obtain a single representative value per cell for group-level statistical analysis. These time windows were applied consistently within each experimental group, and the same definitions were used for statistical analyses and figure presentations.

To test the physiological effects of D2-like receptors on striatopallidal GABAergic transmission, we used the following agonists and antagonists: quinpirole, a DA D2-like receptors agonist ((-)-Quinpirole hydrochloride, 20 nM, 100 nM, 10 μM, Tocris, 1061), DA (Dopamine

hydrochloride, 20 nM, Tocris, 3548), A-412997, a D4R-selective agonist (A-412997 dihydrochloride, 100 nM, Tocris, 4552), and L-741626, a D2R-selective antagonist (L-741,626, 100 nM, Tocris, 1003). For antagonist experiments using L-741626, a lower concentration of quinpirole (100 nM) was used to avoid masking the antagonist effect. These drugs were bath-applied during the recording session after stable baseline IPSC traces were established. To measure the paired pulse ratio (PPR) and ongoing activity of GABA transmission at striatopallidal synapses in the GPe subregions, we optogenetically stimulated striatopallidal axon terminals by using paired light stimuli (50 ms interval) for PPR assessment and trains of 10 light pulses at 20 Hz for ongoing activity, respectively. This interstimulus interval (ISI) was selected based on established protocols for PPR measurement using ChR2[29–31]. For the experiment measuring strontium-induced asynchronous GABA release from striatopallidal synaptic terminals, strontium chloride hexahydrate (4 mM, Sigma-Aldrich, Cat. No. 255521) was added to the ACSF in place of calcium. After recording oIPSCs in normal ACSF, the calcium-containing ACSF was replaced with strontium-containing ACSF. The amplitude and frequency of strontium-induced asynchronous IPSCs were analyzed using Mini Analysis software (Synaptosoft). To quantify the relative suppression level of ongoing activity from individual IPSCs, the charge ratio was calculated using the following equation (1)[29].

$$R_Q = \frac{Q_T}{Amp_1}, Q_T = \frac{\text{Total Charge}_{post}}{\text{Total Charge}_{baseline}}, Amp_1 = \frac{\text{First Amplitude}_{post}}{\text{First Amplitude}_{baseline}} \quad (1)$$

Clustering analysis of strontium miniature responses

To assess whether miniature IPSC features differ systematically across GPe subregions, we performed an unsupervised clustering analysis of strontium-induced miniature responses. This approach allowed us to capture subtle multivariate structure in amplitude, rise time, and decay constant distributions, and to test for region-specific deviations beyond simple univariate comparisons. Strontium mini responses were analyzed using Mini Analysis software (Synaptosoft).

1. **Quantification and statistical analysis**

   Miniature IPSC features {amplitude (AMP), rise time (RT), decay constant (DT)} were merged into a single matrix with corresponding region labels in MATLAB. Miniature responses containing any missing value (NaN) were discarded. Subsequently, outliers whose AMP, RT, or DT fell outside the [0.01, 99.99] percentile of the corresponding

marginal distribution were also discarded. Finally, each feature was z-standardized along each marginal distribution ($\mu = 0$, $\sigma = 1$).

2. **Recursive k-means subclustering**

   To capture substructure without over-fragmentation, we implemented a recursive k-means clustering method (recursiveKMeansAuto). At every cluster, the optimal k ($2 \leq k \leq 10$) was determined with the Calinski–Harabasz (CH) index. A cluster was split only when (i) its size exceeded 500 miniature responses and (ii) the optimal k increased the CH gain ≥ 5 % relative to k = 2. Empirically, the 500 counts threshold guarantees an expected count ≥ 20 for each of the four regions in the subsequent χ^2 test, while the 5% CH increment threshold filters out marginal improvements that are rarely reproducible in biological replicates.

3. **Cluster × region contingency testing**

   For every cluster, a 4 × 2 contingency table was assembled (rows = regions; columns = inside vs. outside *c*). Clusters containing fewer than $n_{\min} = \left\lceil \frac{20}{\min_r p_r} \right\rceil = 167$ spikes (2), where p_r is the global proportion of region r, were excluded so that each region retained an expected count ≥ 20. Tables were evaluated with Pearson's χ^2 (d.f. = 3); standardized residuals $Z_{er} = \frac{O_{cr} - E_{cr}}{\sqrt{E_{cr}}}$ (3) were used to quantify region-specific deviations (excesses or deficits).

4. **Region-wise deviation and pairwise contrasts**

   A region's overall contribution to the global χ^2 statistic was defined as $S_r = \sum_c Z_{cr}^2$ (4). Significance was assessed by randomly permuting region labels 10,000 times. To compare regions directly, we computed ΣZ^2 differences (ΔS) and obtained permutation p-values with the same 10,000 null replicates. Raw p-values were adjusted both by Holm–Bonferroni (controlling the family-wise error rate at 0.05) and by the Benjamini–Hochberg procedure (false-discovery rate 0.05).

5. **Visualization**

   Heat maps depict ΔS values with significant comparisons marked by asterisks (Holm-corrected $p < 0.05$). A normalized bar plot illustrates the magnitude of VL's deviation relative to the other three regions; horizontal bars rank regions by ΣZ^2, annotated with

permutation p values, and a permutation cloud plot overlays observed ΣZ^2 (red stars) on 10,000 null draws (gray).

Biocytin labeling and immunostaining of biocytin-filled neurons

For examining the cell type of the recorded GPe neurons, Cs-based internal solution containing 0.2% biocytin (B4261, Sigma-Aldrich) was loaded into GPe neurons for 20 min. After the delicate retraction of the glass pipette, brain slices were fixed in 4% PFA overnight at 4°C. On the following day, slices were washed with PBS, PBST for 1 hours and blocked with solution containing 10% NGS and 2% BSA for 4 hours. After blocking, brain sections were incubated with an anti-Parvalbumin antibody (guinea pig polyclonal, 1:1000, 195 004, Synaptic Systems) and an anti-FOXP2 antibody (rabbit polyclonal, 1:500, ab16046, Abcam), in blocking solution at 4℃ for 3 days, followed by secondary antibodies (goat anti-rabbit, goat anti-guinea pig, 1:1000, Invitrogen) conjugated to Alexa 594 and Alexa 647 fluorophores and Alexa 405-conjugated streptavidin (1:500, Invitrogen) in blocking solution at 4℃ for 2 days. After washing with PBST and PBS for 12 hours, brain slices were mounted onto slides using a mounting medium (P36934, Invitrogen). Images were obtained by an FV1000 confocal laser scanning microscope (Olympus) and an LSM880 multi-photon confocal laser scanning microscope with airyscan (Carl Zeiss). Recorded neurons were classified as PV-positive or FOXP2-positive based on the colocalization of biocytin labeling with immunostaining signals, which were examined and confirmed using ImageJ[59,62].

Virus purchase

AAV9-hSyn-rDA2h was purchased from WZ Biosciences, with permission from Dr. Yulong Li (Peking University School of Life Sciences). The production titer was 3.28×10^{13} virus molecules/ml. AAV9-Syn-Flex-GCaMP6f-WPRE-SV40 was purchased from Addgene (100833-AAV9). The production titer was 2.20×10^{13} genome copy/ml.

AAV vector production

For adeno-associated virus (AAV)-based synaptophysin expression, we purchased pAAV-hSyn-FLEx-mGFP-2A-Synaptophysin-mRuby (Addgene, #71760), which allows expression of mGFP and Synaptophysin-mRuby in Cre-expressing neurons. AAVs were thereafter purified by iodixanol

gradient ultracentrifugation by the KIST Virus Facility. The production titer of virus was as follows: pAAV-hSyn-FLEx-mGFP-2A-Synaptophysin-mRuby (1.19×10^{13} genome copy/ml).

Stereotaxic viral injection for striatopallidal axon labeling

Stereotaxic virus injections for striatopallidal axon labeling were conducted in Adora2A-Cre mice. Mice were deeply anesthetized by intraperitoneal injection of zoletil (60 mg/kg, Virbac Korea) and rompun (15 mg/kg, Bayer Korea) mixture solution (zoletil : rompun : saline = 4 : 1 : 20) and mounted in a stereotaxic frame (51730, Stoelting). A small hole was drilled after exposing the skull, and AAVs were injected through a glass micropipette with a long, narrow tip (size: 10 – 20 μm), which was fabricated using a micropipette puller (P-1000, Sutter Instrument). The glass pipette was slowly advanced to the coordinates specified for each target area and left in place for 5 min prior to virus injection. The virus solution was injected at an infusion rate of 100 nl/min, and the glass pipette was withdrawn 10 min after the completion of the injection. Following the injection, the scalp was sutured, and the mice were returned to their home cages for a minimum of 21 days before the subsequent experiments. A total volume of 1600 nl virus solution (400 nl per injection site, AAV5-hSyn-Flex-mGFP-2A-Synaptophysin-mRuby) was injected into the striatum (coordinates used, AP: +0.8 mm, ML: ±2.65 mm from the bregma, DV: -4.2 mm and -2.5 mm for the lateral striatum from the exposed dura mater, AP: +0.85 mm, ML: ±2.00 mm from the bregma, DV: -3.2 mm and -1.85 mm for the medial striatum from the exposed dura mater) to achieve sufficient viral expression across the entire population of striatal neurons. Mice injected with the virus were subsequently used for immunohistochemistry 6 weeks post-injection.

Stereotaxic 6-OHDA injection

Stereotaxic 6-OHDA injections were conducted on mice (Adora2A-Cre, Adora2A-Cre;Ai32, and Adora2A-Cre;Ai9) using a stereotaxic system (51730, Stoelting). Before surgery, mice were deeply anesthetized by intraperitoneal injection of zoletil (60 mg/kg, Virbac Korea) and rompun (15 mg/kg, Bayer Korea) mixture solution (zoletil : rompun : saline = 4 : 1 : 20). A total volume of 300 nl 6-OHDA solution (2.5 mg/ml, dissolved in 0.9% sterile saline with 0.02% ascorbic acid) was injected unilaterally into the left MFB (coordinates used, AP: -0.7 mm, ML: +1.2 mm from the bregma, DV: -4.80 mm from the exposed dura mater for mice aged 3 to 4 weeks, AP: -1.2 mm,

ML: +1.2 mm from the bregma, DV: -4.75 mm from the exposed dura mater for mice older than 8 weeks). A glass micropipette with a long, narrow tip (size: 10 – 20 μm) was made using a micropipette puller (P-1000, Sutter Instrument) to deliver 6-OHDA. The glass pipette was slowly advanced to the target area and left in place for 5 min prior to the 6-OHDA injection. 6-OHDA solution was injected at an infusion rate of 100 nl/min, and the glass pipette was withdrawn 10 min after the end of injection. After the injection, the scalp was sutured, and the mice were returned to their home cages. Mice injected with 6-OHDA were used for electrophysiology and immunohistochemistry experiments at 1, 3, 5, and 7 days post-injection[21,87].

Spot detection and synapse extraction analysis

Spot detection and synapse extraction analysis were performed similarly as previously described[21,88,89]. To extract synapses from the acquired images, we implemented a general method for spot detection. The method utilizes mathematical morphological processing based on set theory. Signal enhancement and spot detection can be achieved by treating objects within images as sets and utilizing combinations of logical operators in set theory. This method consists of three steps: denoising, signal enhancement, and spot extraction. In the denoising step, the acquired images are processed using Gaussian filter with σ = 0.5. For signal enhancement, a combination of three thresholding algorithms with top-hat transform, hard thresholding, and Otsu thresholding are applied to the resulting images. Top-hat transform of an image $I(m)$ is represented as equation (5):

$$\mathrm{T}(I(m)) = I(m) - I(m) \circ s(m) \qquad (5)$$

where $\circ$ denotes the opening operator in morphological processing and $s(m)$ denotes the structuring element. Our structuring element $s(m)$ for applying top-hat transform is circular shape with size of 10 X 10. Hard thresholding is expressed as equation (6):

$$\mathrm{H}\big(I(m)\big) = \begin{cases} I(m) & \text{if } I(m) > \text{threshold} \\ 0 & \text{if } I(m) < \text{threshold} \end{cases} \qquad (6)$$

Threshold value of hard thresholding is 45000. After applying top-hat transform and hard thresholding to the acquired images, Otsu's thresholding method is exploited to the processed

images to enhance fluorescent signal from the actual objects while suppressing background noise. From the signal-enhanced images, spots are extracted using a combination of morphological filters, which include two key operations: filling and opening. The filling is used to fill out holes in fluorescent spots, while the opening operation smooths spot contours and removes irrelevant fluorescent signals unrelated to synaptic structures. The extracted spots are clustered within the set of images (presynaptic and postsynaptic) corresponding to distance among the spots, which allows the images to delineate presynaptic and postsynaptic structures. By calculating the distance between presynaptic and postsynaptic clusters, those with a separation of less than 1 pixel (40 nm) were merged to form synapses.

Point pattern analysis

The spatial analysis of clustered features between striatopallidal axon terminals and D2Rs was conducted using Ripley's analysis on both single group and group vs. group scale[90]. Ripley's function describes spatial characteristics of the sample (clustering or dispersion) over a range of distances. The edge corrected Ripley's function is defined as equation (7):

$$K(r) = \lambda^{-1} \sum_{i \neq j} k_{i,j} I(d_{i,j} \leq r)/N \qquad (7)$$

where λ is the density of a point pattern; $k_{i,j}$ is the inverse of a portion of circumference with center at point i and radius r, that lies within the boundary and passes through point j; function I is an indicator function; d is the Euclidean distance between points i and j; N is the number of points in the pattern. A variance stabilized version of the Ripley's K function, defined in equation (8), was used in this study:

$$H_r = \sqrt{\frac{K(r)}{\pi} - r} \qquad (8)$$

Ripley's function was calculated for each observed point pattern. Group vs. group analysis was also used to determine whether point patterns from one group had similar spatial properties with patterns from another (null) group. We assume that all m (the total number of generated patterns)

patterns in the null group are generated using the identical point method.

Diggle-Cressie-Loosmore-Ford (DCLF) test

Diggle-Cressie-Loosmore-Ford (DCLF) test was performed similarly as previously described[21,91]. The DCLF test quantifies the difference between the H function of the observed pattern and the H function for the null group at the given spatial scale. We computed $H(r)$ for the test pattern $H_{\text{obs}}(r)$ and each pattern in the null group $H_i(r)$, then we estimated the summary function $\acute{H}(r)$ for the null group as in equation (9):

$$\acute{H}(r) = \frac{1}{m+1}\left(H_1(r) + H_2(r) + \cdots + H_m(r) + H_{\text{obs}}(r)\right) \qquad (9)$$

Then, the maximum vertical separation between $H(r)$ and $\acute{H}(r)$ is defined as in equation (10):

$$T_{\text{obs}} = \int_0^R (H_{\text{obs}}(r) - \acute{H}(r))^2 \, dr \qquad (10)$$

where R is maximum value of the interaction distance. To compute p-value, the following formula can be used: $p = \frac{\sum_1^m I(T_{\text{obs}} > T_i)}{m+1}$, where $I(T_{\text{obs}} > T_i) = \begin{cases} 1, T_{\text{obs}} > T_i \\ 0, \text{otherwise} \end{cases}$ (11) and T_i is computed between the observed pattern and each pattern in the test group $\left(i = \overline{1,m}\right)$.

Computational model of synaptic transmission

A computational model is based on the Tsodyks-Markram model[47] to simulate synaptic responses and to understand the underlying mechanisms affecting neurotransmitter release probability and synaptic plasticity under different experimental conditions. The model incorporated both facilitation and depression dynamics, adapting established frameworks for synaptic transmission modeling. The following list outlines the key variables and parameters utilized in this modeling approach.

The model included the following key variables:

$u(t)$: Utilization of synaptic resources at time t.

$R(t)$: Fraction of resources in the recovered state at time t.

$n(t)$: Vesicle availability at time t.

$\mathrm{Ca}(t)$: Intracellular calcium concentration at time t.

$P(t)$: Release probability at time t.

$\mathrm{IPSC}(t)$: Inhibitory postsynaptic current at time t.

Key parameters were defined as:

P_0: Baseline release probability.

K_c: Dissociation constant for calcium's effect on release probability.

τ_f: Facilitation time constant.

τ_d: Depression time constant.

τ_rec: Recovery time constant.

τ_Ca: Calcium decay time constant.

$[\mathrm{Ca}]_\mathrm{influx}$: Amplitude of calcium influx during action potentials.

$P_{\mathrm{open}_\mathrm{VGCC}}$: Probability of calcium channel opening.

Mathematical framework

The model was governed by a set of differential equations (equations (12-17)):

1. Calcium dynamics:

$$\frac{\mathrm{dCa}}{\mathrm{d}t} = \frac{\mathrm{Ca} - [\mathrm{Ca_o}]}{\mathrm{d}t} + \delta_\mathrm{spike} \frac{P_{\mathrm{open}_\mathrm{VGCC}} * [\mathrm{Ca}]_\mathrm{influx}}{\tau_\mathrm{ca}} \qquad (12)$$

where $[Ca_o]$= 50 nM[92,93] is the baseline calcium concentration, and δ_{spike} is 1 at spike times and 0 otherwise.

2. Release probability:

$$P(t) = P_0\left(\frac{[\mathrm{Ca}(t)]^m}{K_c^m + [\mathrm{Ca}(t)]^m}\right) \qquad (13)$$

where m = 4 is the Hill coefficient for calcium effect on release probability[94,95].

3. Vesicle availability:

$$\frac{\mathrm{d}n}{\mathrm{d}t} = \frac{n_\infty - n(t)}{\tau_\mathrm{rec}} - \delta_\mathrm{spike} u(t) R(t) n(t) \qquad (14)$$

4. Utilization of synaptic resources:

$$\frac{\mathrm{d}u}{\mathrm{d}t} = -\frac{u(t)}{\tau_\mathrm{f}} + \delta_\mathrm{spike} R(t)(1 - u(t)) \qquad (15)$$

5. Recovery of synaptic resources:

$$\frac{\mathrm{d}R}{\mathrm{d}t} = \frac{1-R(t)}{\tau_{\mathrm{d}}} - \delta_{\mathrm{spike}} u(t) R(t) n(t) \qquad (16)$$

6. Inhibitory postsynaptic current:

$$\mathrm{IPSC}(t) = \mathrm{IPSC}(t) + A(t)\mathrm{e}^{-\frac{t-t_{\mathrm{spike}}}{\tau_{\mathrm{IPSC}}}} \qquad (17)$$

where $A(t) = u(t)R(t)n(t)$ and $\tau_{\mathrm{IPSC}} = 0.02$ is the time constant for IPSC decay.

Simulation protocol

Simulations were conducted over a 1-second duration with a time step of dt = 0.001 seconds. Action potentials were simulated at 0.5 and 0.55 seconds to represent paired-pulse stimulation. The differential equations were numerically integrated using the Euler method. Initial conditions were set based on physiological values, and variables were constrained to remain within plausible biological ranges to prevent computational errors.

Parameter optimization

An optimization routine was employed to fit the model to the experimental PPR data. The objective function minimized the squared difference between the simulated PPR and the observed mean PPR for each condition. The optimization process involved:

1. Control condition: Parameters were initially optimized for the control condition using the differential evolution. To ensure physiological plausibility, bounds were specified for each parameter, and the number of iterations was capped at 100. To accurately capture the synaptic behavior observed in different conditions, the bounds for the baseline release probability (P0) were dynamically adjusted based on the observed paired-pulse ratio (PPR). Specifically, for the facilitating synapses (PPR > 1.05) the bounds for P0 were set to (0.1, 0.5). This range allows P0 to vary within values that support an increasing release probability upon successive stimuli, characteristic of facilitating synapses. For synapses that are non-facilitating or depressing (PPR ≈ 1 or PPR < 1) the bounds for P0 were adjusted to (0.55, 0.9).
2. Quinpirole condition: Starting from the optimized control parameters, scaling factors were introduced to simulate the effect of quinpirole, a dopamine D2 receptor agonist on

the VGCC open probability ($P_{\mathrm{open}_{\mathrm{VGCC}}}$). To isolate the effect of dopamine on synaptic dynamics, we constrained the model such that only the calcium channel open probability was allowed to vary between baseline and quinpirole conditions, consistent with prior evidence that D2-like receptor activation modulates presynaptic calcium influx[96–99]. The optimization aimed to reproduce the observed changes in PPR under quinpirole treatment. In this case the scaling parameter for the $P_{open_{VGCC}}$ was optimized, while the rest of the parameters remained the same as in the optimized 'control conditions'. If the synapses changed from non-facilitating (PPR ≈ 1) to facilitating (PPR > 1) under 'quinpirole condition', the following parameters were manually adjusted to guarantee facilitation.

To ensure robustness and reproducibility of the model fitting, we performed multiple independent optimizations to the mean paired-pulse ratio (PPR) measured under baseline and quinpirole (QP) conditions for each experimental group (control and 6-OHDA). For each condition, the model was fit several times using different random initializations of the full parameter set. This approach was designed to avoid reliance on a single local optimum and to assess whether consistent parameter changes emerge across fits. All fits were performed independently, and only those that produced physiologically plausible values and minimized the squared error between simulated and observed PPR were retained for downstream analysis. This procedure ensured that the reported effects were robust and not dependent on specific fitting trajectories or initial conditions. For the 6-OHDA condition, model parameters were optimized independently using the same procedure described above for the control condition. For the 6-OHDA + quinpirole condition, the model was fit as described for quinpirole, by optimizing a scaling factor on VGCC open probability while keeping all other parameters fixed.

Statistical analysis and exclusion criteria for computational modeling

Statistical comparisons between conditions were performed using non-parametric tests due to the sample size and data distribution. The Wilcoxon Signed-Rank Test was applied for paired comparisons of parameters, and the Mann-Whitney Test was applied for unpaired comparisons within the same cells under different conditions. Cells were excluded from analysis if the simulated PPR under quinpirole did not match the observed behavior (e.g., the model predicted facilitation when depression was observed experimentally, or vice versa).

Model performance evaluation

To assess the quality of model fits, we compared simulated outputs with the corresponding experimental PPR values and Ca^{2+} fluorescence signals across all GPe subregions and conditions (control and DA depletion). Model error was quantified using the mean squared error (MSE) and the root mean squared error (RMSE), defined as the square root of the average squared difference between simulated and experimental PPR values. These metrics provide a direct measure of deviation from experimental targets while retaining biological units. Representative overlays of simulated and experimental IPSC traces, as well as comparisons of simulated versus experimental PPR distributions, were also generated to visually confirm model performance. All numerical values of MSE and RMSE are reported in Table S4.

Software and libraries

All computations were performed using Python 3.9, with key libraries including:

NumPy: For numerical computations and array manipulations.

SciPy: For optimization routines and statistical tests.

Pandas: For data handling and manipulation.

Calcium imaging of striatopallidal axonal boutons in acute brain slices

For imaging cytosolic Ca^{2+} concentration at axonal boutons, Cre-dependent GCaMP6f was expressed across the striatum. AAV9-Syn-Flex-GCaMP6f-WPRE-SV40 was diluted 1:2 in autoclaved PBS immediately before use. A total of 1600 nl virus was injected bilaterally (400 nl per site) at the following coordinates relative to bregma to achieve broad expression across the striatum (coordinates used, AP: +0.8 mm, ML: ±2.65 mm from the bregma, DV: -4.2 mm and -2.5 mm for the lateral striatum from the exposed dura mater, AP: +0.85 mm, ML: ±2.00 mm from the bregma, DV: -3.2 mm and -1.85 mm for the medial striatum from the exposed dura mater). Acute brain slices containing the striatum and GPe were prepared 3 weeks after the viral injection, described in 'Brain slice preparation for electrophysiology' section. For imaging, slices were transferred to a chamber perfused with carbogenated ACSF at 2–3 ml/min using a peristaltic pump (Miniplus 3, Gilson). Ca^{2+} signals were acquired on a A1R MP^{+} confocal microscope (Nikon).

Ca^{2+} images were obtained using a krypton/argon laser (488 nm excitation and > 495 nm emission) and acquired at 2 frames/s with 256 x 256 pixels for ~30 sec. For the evoked synaptic release at the axon terminals, the tungsten bipolar electrode was placed in the striatum and oriented obliquely to align with the presumed trajectory of striatopallidal axon fibers. Synaptic responses were evoked by 20 Hz stimulation (200 μA, 0.1 ms duration for 1.0 sec) via a constant current isolation unit (A365, World Precision Instruments). To assess the effect of D2-like receptor activation on axon-terminal Ca^{2+} signals, 10 μM quinpirole was bath-applied for at least 4 minutes. All the solutions were bubbled with 95% O_2 and 5% CO_2 (pH 7.4). Image sequences were analyzed in MATLAB (MathWorks). We segmented putative boutons by Otsu-based thresholding with user-adjusted contrast and additionally screened by manually to exclude non-punctate or artifactual ROIs. Calcium transients were calculated as $\Delta F/F_0 = (F - F_0) / (F_0 - F_b)$, where F_0 is the baseline fluorescence measured before quinpirole application (Base condition) and F_b is the background fluorescence defined from a manually selected background ROI.

Statistics and reproducibility

All data were analyzed using the following software: Clampfit 10.7 (Molecular Devices), Mini Analysis (version 6.0.7, Synaptosoft), OriginPro 2017 (OriginLab), Zen software (version 2.5, Carl Zeiss), ImageJ (version 1.53c, NIH), and MATLAB (version R2021a, MathWorks). Statistical analyses were performed using GraphPad Prism (version 10, GraphPad software). Summary statistics were presented as either box-and-whisker plots (center line, median; box limits, 25th and 75th percentiles; whiskers, minimum to maximum values) or mean ± SEM. Two-tailed unpaired and paired student's t-tests, one-way ANOVA with two-sided Holm-Sidak's post-hoc multiple comparison test, two-way repeated measures ANOVA with two-sided Holm-Sidak's post-hoc multiple comparison test, two-tailed one-sample t-test, linear regression, and the Kolmogorov-Smirnov test were employed to assess statistical differences (two-sided) between the groups. A P-value of less than 0.05 was considered statistically significant and exact P-values are provided in the legends unless $P < 0.0001$. Significance levels are also denoted as follows: *$p < 0.05$, **$p < 0.01$, ***$p < 0.001$, and ****$p < 0.0001$. Statistical tests were primarily applied to datasets involving discrete group comparisons. Panels such as Fig. 1b,h, Fig. 2e, Fig. 4e,k, and Fig. 7e,f,h present time-course traces, cumulative probability distributions, or computational

simulations. These are provided to show representative biological trends and data distributions; thus, they were excluded from formal group-wise statistical comparisons, with detailed quantitative summaries provided in the associated summary plots. All experiments were independently repeated at least three times with similar results. In the legends, n is defined as the number of technical replicates (e.g., independent slices or cells) followed by the number of independent biological replicates (mice) from which they were derived. For all electrophysiological experiments, the individual cell was defined as the primary unit of statistical analysis to account for the intrinsic physiological variability between neurons. To ensure transparency regarding the hierarchical nature of the data, the number of biological replicates (mice) is explicitly provided alongside the technical replicates in the legends. We did not observe obvious batch effects or systematic differences between cells recorded from the same animal. Sample sizes were not pre-determined by statistical methods but are comparable to those commonly used in the field. Exact statistical values for all main figures are provided in Table S5.

Data availability

Source data are provided with this paper. All numerical data underlying the figures (including simulation outputs) are compiled in the accompanying Source Data Excel file and are archived on Zenodo (DOI: 10.5281/zenodo.18608880).

Code availability

Python and MATLAB code used for data analysis and simulations in this study are publicly available on Zenodo (DOI: 10.5281/zenodo.18608880). The corresponding GitHub repository is available at https://github.com/yelee03153/Striatopallidalsynapse.git

References

1. Kravitz, A. V. *et al.* Regulation of parkinsonian motor behaviours by optogenetic control of basal ganglia circuitry. *Nature* **466**, 622–626 (2010).
2. Arber, S. & Costa, R. M. Connecting neuronal circuits for movement. *Science (80-.).* **360**, 1403–1404 (2018).
3. Roth, R. H. & Ding, J. B. Cortico-basal ganglia plasticity in motor learning. *Neuron* **112**, 2486–2502 (2024).
4. Gerfen, C. R. Molecular effects of dopamine on striatal-projection pathways. *Trends Neurosci.* **23**, 64–70 (2000).
5. Kreitzer, A. C. & Malenka, R. C. Striatal Plasticity and Basal Ganglia Circuit Function. *Neuron* **60**, 543–554 (2008).
6. Hedreen, J. C. Tyrosine hydroxylase-immunoreactive elements in the human globus pallidus and subthalamic nucleus. *J. Comp. Neurol.* **409**, 400–410 (1999).
7. Smith, Y. & Kieval, J. Z. Anatomy of the dopamine system in the basal ganglia. *Trends Neurosci.* **23**, 28–33 (2000).
8. Meszaros, J. *et al.* Evoked transients of ph-sensitive fluorescent false neurotransmitter reveal dopamine hot spots in the globus pallidus. *Elife* **7**, 1–19 (2018).
9. Lindvall, O. & Björklund, A. Dopaminergic innervation of the globus pallidus by collaterals from the nigrostriatal pathway. *Brain Res.* **172**, 169–173 (1979).
10. Mamad, O., Delaville, C., Benjelloun, W. & Benazzouz, A. Dopaminergic control of the globus pallidus through activation of D2 receptors and its impact on the electrical activity of subthalamic nucleus and substantia nigra reticulata neurons. *PLoS One* **10**, 1–16 (2015).
11. Marjorie A. Ariano, Jean Wang, Kurtis L. Noblett, Eric R.Larson, D. R. S. Cellular distribution of the rat D4 dopamine receptor protein in t anti-receptor antisera. *Brain Res.* **752**, 26–34 (1997).
12. Mauger, C. *et al.* Development and characterization of antibodies directed against the mouse D4 dopamine receptor. *Eur. J. Neurosci.* **10**, 529–537 (1998).
13. Shin, R. M. *et al.* Dopamine D4 Receptor-Induced Postsynaptic Inhibition of GABAergic Currents in Mouse Globus Pallidus Neurons. *J. Neurosci.* **23**, 11662–11672 (2003).

14. Foster, N. N. *et al.* The mouse cortico–basal ganglia–thalamic network. *Nature* **598**, 188–194 (2021).
15. Lee, J., Wang, W. & Sabatini, B. L. Anatomically segregated basal ganglia pathways allow parallel behavioral modulation. *Nat. Neurosci.* **23**, 1388–1398 (2020).
16. Smith, Y., Lavoie, B., Dumas, J. & Parent, A. Evidence for a distinct nigropallidal dopaminergic projection in the squirrel monkey. *Brain Res.* **482**, 381–386 (1989).
17. Fuchs, H. & Hauber, W. Dopaminergic innervation of the rat globus pallidus characterized by microdialysis and immunohistochemistry. *Exp. Brain Res.* **154**, 66–75 (2004).
18. Patriarchi, T. *et al.* Ultrafast neuronal imaging of dopamine dynamics with designed genetically encoded sensors. *Science (80-.).* **360**, (2018).
19. Sun, F. *et al.* A Genetically Encoded Fluorescent Sensor Enables Rapid and Specific Detection of Dopamine in Flies, Fish, and Mice. *Cell* **174**, 481-496.e19 (2018).
20. Zhuo, Y. *et al.* Improved green and red GRAB sensors for monitoring dopaminergic activity in vivo. *Nat. Methods* **21**, 680–691 (2024).
21. Kim, H. J. *et al.* GABAergic-like dopamine synapses in the brain. *Cell Rep.* **42**, 113239 (2023).
22. Cooper, A. J. & Stanford, I. M. Dopamine D2 receptor mediated presynaptic inhibition of striatopallidal GABAA IPSCs in vitro. *Neuropharmacology* **41**, 62–71 (2001).
23. Watanabe, K., Kita, T. & Kita, H. Presynaptic actions of D2-like receptors in the rat cortico-striato-globus pallidus disynaptic connection in vitro. *J. Neurophysiol.* **101**, 665–671 (2009).
24. Zych, S. M. & Ford, C. P. Divergent properties and independent regulation of striatal dopamine and GABA co-transmission. *Cell Rep.* **39**, 110823 (2022).
25. Yamamoto, K. & Kobayashi, M. Opposite roles in short-term plasticity for N-type and P/Q-type voltage-dependent calcium channels in gabaergic neuronal connections in the rat cerebral cortex. *J. Neurosci.* **38**, 9814–9828 (2018).
26. Sims, R. E., Woodhall, G. L., Wilson, C. L. & Stanford, I. M. Functional characterization of GABAergic pallidopallidal and striatopallidal synapses in the rat globus pallidus in vitro. *Eur. J. Neurosci.* **28**, 2401–2408 (2008).
27. Perez-Rosello, T. *et al.* Enhanced striatopallidal gamma-aminobutyric acid (GABA)A receptor transmission in mouse models of huntington's disease. *Mov. Disord.* **34**, 684–696

(2019).

28. Bevan, M. D. Selective innervation of neostriatal interneurons by a subclass of neuron in the globus pallidus of the rat. *J. Neurosci.* **18**, 9438–9452 (1998).
29. Burke, K. J., Keeshen, C. M. & Bender, K. J. Two Forms of Synaptic Depression Produced by Differential Neuromodulation of Presynaptic Calcium Channels. *Neuron* **99**, 969-984.e7 (2018).
30. Sciamanna, G., Ponterio, G., Mandolesi, G., Bonsi, P. & Pisani, A. Optogenetic stimulation reveals distinct modulatory properties of thalamostriatal vs corticostriatal glutamatergic inputs to fast-spiking interneurons. *Sci. Rep.* **5**, 1–15 (2015).
31. Pradier, X. B. *et al.* Long-Term Depression Induced by Optogenetically Driven Nociceptive Inputs to Trigeminal Nucleus Caudalis or Headache Triggers. **38**, 7529–7540 (2018).
32. Liu, C., Kershberg, L., Wang, J., Schneeberger, S. & Kaeser Correspondence, P. S. Dopamine Secretion Is Mediated by Sparse Active Zone-like Release Sites In Brief Secretion of dopamine requires specialized release machinery. *Cell* **172**, 706-709.e15 (2018).
33. Kershberg, L., Banerjee, A. & Kaeser, P. S. Protein composition of axonal dopamine release sites in the striatum. *Elife* **11**, 1–29 (2022).
34. Kim, H. J. *et al.* GABAergic-like dopamine synapses in the brain. *Cell Rep.* **42**, 113239 (2023).
35. Ding, J., Peterson, J. D. & Surmeier, D. J. Corticostriatal and thalamostriatal synapses have distinctive properties. *J. Neurosci.* **28**, 6483–6492 (2008).
36. Kaeser, P. S. & Regehr, W. G. The readily releasable pool of synaptic vesicles. *Curr. Opin. Neurobiol.* **43**, 63–70 (2017).
37. Katayama, S. *et al.* Slowly progressive L-DOPA nonresponsive pure akinesia due to nigropallidal degeneration: A clinicopathological case study. *J. Neurol. Sci.* **161**, 169–172 (1998).
38. Tan, W. Q. *et al.* Deterministic Tractography of the Nigrostriatal-Nigropallidal Pathway in Parkinson's Disease. *Sci. Rep.* **5**, 2–7 (2015).
39. Parent, A., Lavoie, B., Smith, Y. & Bédard, P. The dopaminergic nigropallidal projection in primates: distinct cellular origin and relative sparing in MPTP-treated monkeys. *Adv.*

Neurol. **53**, 111–116 (1990).

40. Jones, J. A., Higgs, M. H., Olivares, E., Peña, J. & Wilson, C. J. Spontaneous Activity of the Local GABAergic Synaptic Network Causes Irregular Neuronal Firing in the External Globus Pallidus. *J. Neurosci.* **43**, 1281–1297 (2023).
41. Mallet, N., Delgado, L., Chazalon, M., Miguelez, C. & Baufreton, J. Cellular and synaptic dysfunctions in Parkinson's disease: Stepping out of the striatum. *Cells* **8**, 1–29 (2019).
42. Galvan, A. & Wichmann, T. Pathophysiology of Parkinsonism. *Clin. Neurophysiol.* **119**, 1459–1474 (2008).
43. Cui, Q. *et al.* Blunted mGluR Activation Disinhibits Striatopallidal Transmission in Parkinsonian Mice. *Cell Rep.* **17**, 2431–2444 (2016).
44. Kiskowski, M. A., Hancock, J. F. & Kenworthy, A. K. On the use of Ripley's K-function and its derivatives to analyze domain size. *Biophys. J.* **97**, 1095–1103 (2009).
45. Rebola, N. *et al.* Distinct Nanoscale Calcium Channel and Synaptic Vesicle Topographies Contribute to the Diversity of Synaptic Function. *Neuron* 1–18 (2019). doi:10.1016/j.neuron.2019.08.014
46. N Bert Loosmore, E. D. F. Statistical inference using the g or K point pattern spatial statistics. *Ecology* **87**, 1925–1931 (2006).
47. Tsodyks, M. V. & Markram, H. The neural code between neocortical pyramidal neurons depends on neurotransmitter release probability. *Proc. Natl. Acad. Sci. U. S. A.* **94**, 719–723 (1997).
48. Markram, H., Wang, Y. & Tsodyks, M. Differential signaling via the same axon of neocortical pyramidal neurons. *Proc. Natl. Acad. Sci. U. S. A.* **95**, 5323–5328 (1998).
49. Kisilevsky, A. E. & Zamponi, G. W. D2 dopamine receptors interact directly with N-type calcium channels and regulate channel surface expression levels. *Channels* **2**, 269–277 (2008).
50. Scarnati, M. S., Clarke, S. G., Pang, Z. P. & Paradiso, K. G. Presynaptic Calcium Channel Open Probability and Changes in Calcium Influx Throughout the Action Potential Determined Using AP-Waveforms. *Front. Synaptic Neurosci.* **12**, 1–18 (2020).
51. Shafiei, G. *et al.* Dopamine Signaling Modulates the Stability and Integration of Intrinsic Brain Networks. *Cereb. Cortex* **29**, 1–13 (2019).

52. Barroso-Flores, J., Herrera-Valdez, M. A., Lopez-Huerta, V. G., Galarraga, E. & Bargas, J. Diverse short-term dynamics of inhibitory synapses converging on Striatal projection neurons: Differential changes in a rodent model of Parkinson's disease. *Neural Plast.* **2015**, (2015).

53. Mastro, K. J., Bouchard, R. S., Holt, H. A. K. & Gittis, A. H. Transgenic mouse lines subdivide external segment of the globus pallidus (GPe) neurons and reveal distinct GPe output pathways. *J. Neurosci.* **34**, 2087–2099 (2014).

54. Beier, K. T. *et al.* Rabies screen reveals GPe control of cocaine-triggered plasticity. *Nature* **549**, 345–350 (2017).

55. Dodson, P. D. *et al.* Distinct developmental origins manifest in the specialized encoding of movement by adult neurons of the external globus pallidus. *Neuron* **86**, 501–513 (2015).

56. Mastro, K. J. *et al.* Cell-specific pallidal intervention induces long-lasting motor recovery in dopamine-depleted mice. *Nat. Neurosci.* **20**, 815–823 (2017).

57. Jeon, H. *et al.* Topographic connectivity and cellular profiling reveal detailed input pathways and functionally distinct cell types in the subthalamic nucleus. *Cell Rep.* **38**, 110439 (2022).

58. Abdi, A. *et al.* Prototypic and arkypallidal neurons in the dopamine-intact external globus pallidus. *J. Neurosci.* **35**, 6667–6688 (2015).

59. Dong, J., Hawes, S., Wu, J., Le, W. & Cai, H. Connectivity and Functionality of the Globus Pallidus Externa Under Normal Conditions and Parkinson's Disease. *Front. Neural Circuits* **15**, 1–19 (2021).

60. Xu, Z. *et al.* Deep brain stimulation alleviates Parkinsonian motor deficits through desynchronizing GABA release in mice. *Nat. Commun.* **16**, 1–18 (2025).

61. Spix, T. A. *et al.* Population-specific neuromodulation prolongs therapeutic benefits of deep brain stimulation. *Science (80-.).* **374**, 201–206 (2021).

62. Abrahao, K. P. & Lovinger, D. M. Classification of GABAergic neuron subtypes from the globus pallidus using wild-type and transgenic mice. *J. Physiol.* **596**, 4219–4235 (2018).

63. Ketzef, M. & Silberberg, G. Differential Synaptic Input to External Globus Pallidus Neuronal Subpopulations In Vivo. *Neuron* **109**, 516-529.e4 (2021).

64. Courtney, C. D., Pamukcu, A. & Chan, C. S. Cell and circuit complexity of the external

globus pallidus. *Nat. Neurosci.* **26**, 1147–1159 (2023).

65. Abrahao, K. P., Chancey, J. H., Chan, C. S. & Lovinger, D. M. Ethanol-Sensitive Pacemaker Neurons in the Mouse External Globus Pallidus. *Neuropsychopharmacology* **42**, 1070–1081 (2017).
66. Wang, X., Zhong, P. & Yan, Z. Dopamine D4 modulate GABAergic Signaling in Pyramidl Neurons.PDF. *J. Neurosci.* **22**, 9185–9193 (2002).
67. Lindgren, N. *et al.* Distinct roles of dopamine D2L and D2S receptor isoforms in the regulation of protein phosphorylation at presynaptic and postsynaptic sites. *Proc. Natl. Acad. Sci. U. S. A.* **100**, 4305–4309 (2003).
68. Alessandro Usiello, Ja-Hyun Baik, FrancËoise RougeÂ-Pont, Roberto Picetti, AndreÂe Dierich, Marianne LeMeur, P. V. P. & E. B. Distinct functions of the two isoforms of dopamine D2 receptors. *Nature* **408**, 199–203 (2000).
69. Wang, Y. *et al.* Heterogeneity in the pyramidal network of the medial prefrontal cortex. *Nat. Neurosci. 2006 94* **9**, 534–542 (2006).
70. Bao, J., Reim, K. & Sakaba, T. Target-Dependent Feedforward Inhibition Mediated by Short-Term Synaptic Plasticity in the Cerebellum. *J. Neurosci.* **30**, 8171–8179 (2010).
71. Afia B. Ali and Alex M. Thomson. Facilitating pyramid to horizontal oriens—alveus interneuroneinputs: dual intracellular recordings in slices of rathippocampus. *Journal of physiology* 185–199 (1998).
72. Wong, H. H. W., Watt, A. J. & Sjöström, P. J. Synapse-specific burst coding sustained by local axonal translation. *Neuron* **112**, 264-276.e6 (2024).
73. Lisman, J. E. Bursts as a unit of neural information: Making unreliable synapses reliable. *Trends Neurosci.* **20**, 38–43 (1997).
74. Blackman, A. V., Abrahamsson, T., Costa, R. P., Lalanne, T. & Sjöström, P. J. Target-cell-specific short-term plasticity in local circuits. *Front. Synaptic Neurosci.* **5**, 1–13 (2013).
75. Lehéricy, S. *et al.* Diffusion tensor fiber tracking shows distinct corticostriatal circuits in humans. *Ann. Neurol.* **55**, 522–529 (2004).
76. Lee, J. H., Kim, D. S., Baik, S. K. & Nam, S. O. Nigropallidal iron accumulation in pantothenate kinase-associated neurodegeneration demonstrated by susceptibility-weighted imaging. *J. Neurol.* **257**, 661–662 (2010).

77. Brichta, L. & Greengard, P. Molecular determinants of selective dopaminergic vulnerability in Parkinson's disease: An update. *Front. Neuroanat.* **8**, 122879 (2014).

78. Carmichael, K. *et al.* Function and Regulation of ALDH1A1-Positive Nigrostriatal Dopaminergic Neurons in Motor Control and Parkinson's Disease. *Front. Neural Circuits* **15**, 644776 (2021).

79. Matthias H. Hennig. Theoretical models of synaptic short term plasticity. *Comput. Neurosci.* **7**, (2013).

80. Wei, W. *et al.* Supersensitive presynaptic dopamine D2 receptor inhibition of the striatopallidal projection in nigrostriatal dopamine-deficient mice. *J. Neurophysiol.* **110**, 2203–2216 (2013).

81. Nambu, A. & Tachibana, Y. Mechanism of parkinsonian neuronal oscillations in the primate basal ganglia: Some considerations based on our recent work. *Front. Syst. Neurosci.* **8**, 67336 (2014).

82. Rebola, N. *et al.* Distinct Nanoscale Calcium Channel and Synaptic Vesicle Topographies Contribute to the Diversity of Synaptic Function. *Neuron* **104**, 693-710.e9 (2019).

83. Lycas, M. D. *et al.* Nanoscopic dopamine transporter distribution and conformation are inversely regulated by excitatory drive and D2 autoreceptor activity. *Cell Rep.* **40**, 111431 (2022).

84. Onishi, T., Sakamoto, H., Namiki, S. & Hirose, K. The Altered Supramolecular Structure of Dopamine D2 Receptors in Disc1-deficient Mice. *Sci. Rep.* **8**, 1–8 (2018).

85. Venton, B. J. & Cao, Q. Fundamentals of fast-scan cyclic voltammetry for dopamine detection. *Analyst* **145**, 1158–1168 (2020).

86. Kang, Y. *et al.* Enhanced Dopamine Sensitivity Using Steered Fast-Scan Cyclic Voltammetry. *ACS Omega* **6**, 33599–33606 (2021).

87. Kim, H. Y. *et al.* PLCγ1 in dopamine neurons critically regulates striatal dopamine release via VMAT2 and synapsin III. *Exp. Mol. Med.* **55**, 2357–2375 (2023).

88. Aishwarya, N., Phamila, Y. A. V. & Amutha, R. Multi-focus image fusion using multi-structure top-hat transform and image variance. *Int. Conf. Commun. Signal Process. ICCSP 2013 - Proc.* 352–356 (2013). doi:10.1109/iccsp.2013.6577073

89. Kimori, Y., Baba, N. & Morone, N. Extended morphological processing: A practical

method for automatic spot detection of biological markers from microscopic images. *BMC Bioinformatics* **11**, (2010).

90. Ripley, B. D. Modelling Spatial Patterns. **39**, 172–212 (1977).
91. Baddeley, A. *et al.* On tests of spatial pattern based on simulation envelopes. *Ecol. Monogr.* **84**, 477–489 (2014).
92. Usowicz, M. M., Sugimori, M., Cherksey, B. & Llinás, R. P-type calcium channels in the somata and dendrites of adult cerebellar purkinje cells. *Neuron* **9**, 1185–1199 (1992).
93. Neher, E. Vesicle pools and Ca2+ microdomains: New tools for understanding their roles in neurotransmitter release. *Neuron* **20**, 389–399 (1998).
94. Dodge, F. A. & Rahamimoff, R. Co-operative action of calcium ions in transmitter release at the neuromuscular junction. *J. Physiol.* **193**, 419–432 (1967).
95. Augustine, George J. Milton P. Charlton, S. J. S. & Howard. Calcium action in synaptic transmitter release. *Annu. Rev. Neurosci.* **10th**, 633–693 (1987).
96. Hernádez-López, S. *et al.* D2 dopamine receptors in striatal medium spiny neurons reduce L-type Ca2+ currents and excitability via a novel PLCβ1-IP3-Calcineurin-signaling cascade. *J. Neurosci.* **20**, 8987–8995 (2000).
97. De Waard, M. *et al.* Direct binding of G-protein betagamma complex to voltage-dependent calcium channels. *Nature* **385**, 446–450 (1997).
98. Qin, N., Platano, D., Olcese, R., Stefani, E. & Birnbaumer, L. Direct interaction of Gβγ with a C-terminal Gβγ-binding domain of the Ca2+ channel α1 subunit is responsible for channel inhibition by G protein-coupled receptors. *Proc. Natl. Acad. Sci. U. S. A.* **94**, 8866–8871 (1997).
99. Zamponi, G. W., Bourinet, E., Nelson, D., Nargeot, J. & Snutch, T. P. Crosstalk between G proteins and protein kinase C mediated by the calcium channel α1 subunit. *Nature* **385**, 442–446 (1997).
100. Bollmann, J. H., Sakmann, B. & Borst, J. G. G. Calcium sensitivity of glutamate release in a calyx-type terminal. *Science (80-.).* **289**, 953–957 (2000).
101. Zucker, R. S. & Regehr, W. G. Short-term synaptic plasticity. *Annu. Rev. Physiol.* **64**, 355–405 (2002).
102. Schneggenburger, R. & Erwin Neher. Intracellular calcium dependence of transmitter

release rates at a fast central synapse. *Nature* **406**, 889–893 (2000).

Acknowledgements

The authors express their gratitude to Dr. Taegon Kim, Dr. Hyoung-Ro Lee, and Dr. Suk-Ho Lee for their scientific advice and helpful discussions. The authors also express their gratitude to the members of Kim laboratory for their insightful discussions. This research was supported by the Mid-Career Researcher Program (NRF-2023R1A2C1006489 / RS-2023-NR076777 to JIK) and the Bio & Medical Technology Development Program (NRF-2021M3A9G8022960 / RS-2021-NR056530, NRF-2022M3E5E8017907 / RS-2022-NR067826 to JIK) of the National Research Foundation (NRF) funded by the Korean government (MSIT). This research was also supported by the Institute for Basic Science (IBS-R022-D1 to KM) and the Samsung Future Technology Promotion Project (Project No.: SRFC-IT2302-02). All schematics are author-generated graphics (Adobe Illustrator 2021), with BioRender.com-generated panels used under a BioRender publication license (Created in BioRender. Fig. 4b: Kim, Y., researcher in Dr. Jae-Ick Kim's lab (2026) https://BioRender.com/c4pdiw1; Fig. 4g: Kim, Y., researcher in Dr. Jae-Ick Kim's lab (2026) https://BioRender.com/askeis2; Fig. 8a: Kim, Y., researcher in Dr. Jae-Ick Kim's lab (2026) https://BioRender.com/4844a9w).

Author contributions

Conceptualization: YLL, JIK

Methodology: YLL, MR, KJK, HJK, MJ, YK (Youngjong Kwak), KM, YL, SEL, DPJ, CJL, JIK

Investigation: YLL, MR, YK (Yemin Kim), EC, JIK

Interpretation of Data: YLL, MR, CJL, CL, JIK

Writing - Original Draft: YLL, JIK

Writing - Review and Editing: YLL, MR, CL, JIK

Funding Acquisition: KM, JIK

Supervision: JIK

Competing Interests

The authors declare no competing interests.

Figures and figure legends

Fig. 1 | DA axons capable of releasing DA innervate the GPe with regional heterogeneity

a, Schematic illustration of nigropallidal and striatopallidal pathways (left). The fluorescence image of dopaminergic pathways (right) is representative of 3 independent biological replicates (mice) with similar results. **b**, $GRAB_{DA}$ (rDA2h) fluorescence responses in response to ten electrical pulses (left). A summary of the peak fluorescence changes in three brain regions in brain slices (right) (n (slices/mice): GPe (15/4), M1 cortex (15/4), DLS (22/4)). **c**, Schematic illustrations of the GPe subregions and representative confocal images showing TH+ nigropallidal and RFP+ striatopallidal axons in the GPe subregions of Adora2A-Cre;Ai9 mice. The fluorescence image is representative of 3 independent biological replicates (mice) with similar results. **d**, Quantification of RFP+ areas in the GPe subregions (n (images/mice): (18/3) per GPe subregion, one-way ANOVA; $p = 0.3612$). **e**, Summary statistics of TH+ area in the lateral and medial GPe subregions (left) and in the dorsal and ventral GPe subregions (right) (n (images/mice): (36/6) per each group, two-tailed unpaired t-test; lateral-medial, $p = 0.0013$; dorsal-ventral, $p < 0.0001$). **f**, Quantification of TH+ areas in the GPe subregions (n (images/mice): (18/3) per GPe subregion, ordinary two-way ANOVA with two-sided Holm-Sidak's post-hoc multiple comparisons test; DV axis effect, $p < 0.0001$, LM axis effect, $p = 0.0003$, interaction, $p = 0.8713$). **g**, $GRAB_{DA}$ (rDA2h) fluorescence responses to ten electrical pulses in the GPe subregions. **h**, A summary of the peak fluorescence changes in the GPe subregions in brain slices (n (slices/mice): DL (9/4), VL (10/4), DM (6/4), VM (10/4)). **i**, Summary statistics of the peak fluorescence changes in the GPe subregions in brain slices (n (slices/mice): DL (9/4), VL (10/4), DM (6/4), VM (10/4), one-way ANOVA; $p = 0.3875$). The data are presented as box-and-whisker plots (center line, median; box limits, 25th and 75th percentiles; whiskers, minimum to maximum values) or mean ± SEM. *$p < 0.05$, **$p < 0.01$, ****$p < 0.0001$.

Fig. 2 | DA D2-like receptors modulate striatopallidal transmission through distinct mechanisms within the subregions of the GPe

a, Illustration depicting electrophysiological recording of striatopallidal synaptic transmission via optogenetic stimulation. **b**, Summary statistics of oIPSCs in GPe neurons during bath application

of quinpirole (10 μM) (n (cells/mice): (40/26), two-tailed one-sample t-test; QP ON, $p < 0.0001$, QP OFF, $p < 0.0001$). **c**, Summary statistics of the absolute (left) and normalized values (right) of PPRs (n (cells/mice): (40/26); left, repeated measures one-way ANOVA with two-sided Holm-Sidak's post-hoc multiple comparisons test, $p < 0.0001$; right, two-tailed one-sample t-test, QP ON, $p < 0.0001$, QP OFF, $p = 0.0004$). **d**, Summary statistics of the normalized values of PPRs between the DL/VM and VL/DM GPe subgroup (n (cells/mice): DL/VM (20/17), VL/DM (20/16), two-tailed unpaired t-test; $p = 0.0112$). **e-h**, Illustrations of the GPe subregions (top left), representative recording traces (bottom left), oIPSC amplitude (top center) and PPR plots (bottom center) normalized to baseline, and summary statistics of normalized oIPSCs (top right) and normalized PPRs (bottom right), (n (cells/mice): DL (10/9), VL (10/8), DM (10/8), VM (10/8), two-tailed one-sample t-test). **e,** Summary statistics of normalized oIPSCs (QP ON, $p < 0.0001$, QP OFF, $p < 0.0001$) and PPRs (QP ON, $p = 0.0058$, QP OFF, $p = 0.0051$) in the DL GPe. **f**, Summary statistics of normalized oIPSCs (QP ON, $p < 0.0001$, QP OFF, $p < 0.0001$) and PPRs (QP ON, $p = 0.1166$, QP OFF, $p = 0.1567$) in the DM GPe. **g**, Summary statistics of normalized oIPSCs (QP ON, $p < 0.0001$, QP OFF, $p < 0.0001$) and PPRs (QP ON, $p = 0.1934$, QP OFF, $p = 0.2657$) in the VL GPe. **h**, Summary statistics of normalized oIPSCs (QP ON, $p < 0.0001$, QP OFF, $p < 0.0001$) and PPRs (QP ON, $p = 0.0055$, QP OFF, $p = 0.0694$) in the VM GPe. Data from the entire epoch were averaged for each cell to yield a single value for group-level statistical analysis. The data are presented as box-and-whisker plots (center line, median; box limits, 25th and 75th percentiles; whiskers, minimum to maximum values) or mean ± SEM. *$p < 0.05$, **$p < 0.01$, ***$p < 0.001$, ****$p < 0.0001$.

Fig. 3 | Region-specific dopaminergic modulation of striatopallidal synaptic transmission in the GPe is driven by differential contributions of presynaptic D2Rs and postsynaptic D4Rs

a-d, Schematic illustrations of the GPe subregions and representative recording traces of optogenetically evoked asynchronous GABA release (quantal transmission) in Adora2A-Cre;Ai32 mice during bath application of strontium (4 mM) and quinpirole (10 μM) (left). Summary statistics of quantal oIPSC amplitude and frequency (right), (n (cells/mice): DL (8/6), VL (7/7), DM (16/15), VM (9/8), two-tailed paired t-test). **a**, Summary statistics of quantal oIPSC amplitude ($p = 0.0181$) and frequency ($p = 0.0221$) in the DL GPe. **b**, Summary statistics of quantal oIPSC

amplitude (p = 0.0155) and frequency (p = 0.6242) in the DM GPe. **c**, Summary statistics of quantal oIPSC amplitude (p = 0.0141) and frequency (p = 0.3325) in the VL GPe. **d**, Summary statistics of quantal oIPSC amplitude (p = 0.0007) and frequency (p = 0.001) in the VM GPe. **e**, Cumulative plots of inter-event intervals for quantal oIPSCs at striatopallidal synapses. **f**, Summary statistics of the normalized values of quantal amplitude (n (cells/mice): DL/VM GPe (17/14), VL/DM GPe (23/22), two-tailed unpaired t-test; p = 0.15) (left) and quantal frequency (n (cells/mice): DL/VM GPe (17/14), VL/DM GPe (23/22), two-tailed unpaired t-test; p = 0.0005) (right) between the DL/VM GPe subgroup and VL/DM GPe subgroup during bath application of quinpirole (10 μM). **g**,**i**, Schematic illustrations and representative recording traces of optogenetically evoked oIPSCs in the DL and VM GPe during bath application of L-741626 (100 nM) and quinpirole (100 nM). **h**, Normalized oIPSC amplitude plot and summary statistics in the DL GPe (n (cells/mice): (7/5), two-tailed one-sample t-test; p = 0.0003) (left). Normalized PPR plot and summary statistics in the DL GPe (n (cells/mice): (7/5), two-tailed one-sample t-test; p = 0.3717) (right). **j**, Normalized oIPSC amplitude plot and summary statistics in the VM GPe (n (cells/mice): (7/4), two-tailed one-sample t-test; p = 0.004) (left). Normalized PPR plot and summary statistics in the VM GPe (n (cells/mice): (7/4), two-tailed one-sample t-test; p = 0.4755). The data are presented as box-and-whisker plots (center line, median; box limits, 25th and 75th percentiles; whiskers, minimum to maximum values) or mean ± SEM. *p < 0.05, **p < 0.01, ***p < 0.001.

Fig. 4 | The distinct spatial localization and distribution of presynaptic D2Rs and postsynaptic D4Rs in the GPe subregions may contribute to the region-specific dopaminergic modulation of striatopallidal transmission

a, A schematic illustration describing the injection of AAV5-hSyn-Flex-mGFP-2A-Synaptophysin-mRuby virus into the striatum of Adora2A-Cre mice to selectively label striatopallidal axons and terminals. **b**, A schematic illustration depicting fluorescently labeled striatopallidal axons (GFP), axon terminals (RFP), and D2Rs on iMSNs. **c**, Representative enhanced confocal images of striatopallidal axons, axon terminals, and D2Rs in the GPe subregions. **d**, Summary statistics of D2R+ area (n (images/mice): (95/9) per GPe subgroup, two-tailed unpaired t-test; p = 0.002), D2R+ area colocalized with RFP+ area (n (images/mice): DL-VM GPe (95/9), VL-DM GPe (93/9), two-tailed unpaired t-test; p = 0.0075), D2R+ area

colocalized with GFP+ area (n (images/mice): DL-VM GPe (76/9), VL-DM GPe (108/9), two-tailed unpaired t-test; p = 0.0163), D2R+ area colocalized with GFP+ or RFP+ area (n (images/mice): DL-VM GPe (92/9), VL-DM GPe (103/9), two-tailed unpaired t-test; p = 0.0415), and GFP+ area (n (images/mice): DL-VM GPe (96/9), VL-DM GPe (99/9), two-tailed unpaired t-test; p = 0.2423). **e**, Cumulative plots for the nearest neighbor distance from striatopallidal axon terminals (RFP+) to D2Rs on striatopallidal axons or axon terminals (D2R+ RFP+ or D2R+ GFP+) (n (images/mice): DL-VM GPe (92/9), VL-DM GPe (103/9)). **f**, A schematic illustration depicting fluorescently labeled striatopallidal axons (RFP) in the GPe, projected from iMSNs of Adora2A-Cre;Ai9 mice. **g**, A schematic illustration describing fluorescently labeled striatopallidal axons (RFP), $GABA_A$Rs, and D4Rs in the GPe of Adora2A-Cre;Ai9 mice. **h**, Representative enhanced confocal images, restructured 3D images by IMARIS, and centerpoints of $GABA_A$Rs and D4Rs in the GPe subregions. **i**, Summary statistics of D4R+ fluorescence volume (n (images/mice): DL-VM GPe (47/6), VL-DM GPe (52/6), two-tailed unpaired t-test; p = 0.0031) and number (p < 0.0001). **j**, Summary statistics of $GABA_A$R+ fluorescence volume (n (images/mice): DL-VM GPe (47/6), VL-DM GPe (52/6), two-tailed unpaired t-test; p = 0.9442) and number (p = 0.9979). **k**, Cumulative plots for the nearest neighbor distance from postsynaptic $GABA_A$Rs to postsynaptic D4Rs in the GPe. The data are presented as box-and-whisker plots (center line, median; box limits, 25th and 75th percentiles; whiskers, minimum to maximum values). *p < 0.05, **p < 0.01, ****p < 0.0001.

Fig. 5 | Pre- and postsynaptic DA receptors fine-tune ongoing activity in the GPe through region-specific modulations

a,**d**,**g**,**j**, Schematic illustrations of the GPe subregions (left) and representative recording traces of optogenetically evoked oIPSCs (right), generated by ten light pulses at 20 Hz before and after bath application of quinpirole (10 μM). **b**,**e**,**h**,**k**, Summary plots of ongoing activity in the GPe subregions (n (cells/mice): DL (15/13), VL (15/13), DM (16/14), VM (17/15), repeated measures two-way ANOVA with two-sided Holm-Sidak's post-hoc multiple comparisons test; pulse train: DL, p < 0.0001, VL, p < 0.0001, DM, p < 0.0001, VM, p < 0.0001, QP treatment: DL, p = 0.0001, VL, p = 0.1211, DM, p = 0.6445, VM, p = 0.0021, interaction: DL, p < 0.0001, VL, p = 0.573, DM, p = 0.3497, VM, p < 0.0001). **c,f,i,l,** Summary statistics of oIPSC amplitude peak ratios for

comparative analysis between P2/P1 and P10/P1 in the GPe subregions (n (cells/mice): DL (15/13), VL (15/13), DM (16/14), VM (17/15), repeated measures two-way ANOVA with two-sided Holm-Sidak's post-hoc multiple comparisons test; QP treatment: DL, $p = 0.0003$, VL, $p = 0.5132$, DM, $p = 0.8014$, VM, $p < 0.0001$, peak ratio: DL, $p < 0.0001$, VL, $p < 0.0001$, DM, $p = 0.6871$, VM, $p < 0.0001$, interaction: DL, $p = 0.0648$, VL, $p = 0.2939$, DM, $p = 0.3852$, VM, $p = 0.1611$). **m**, Summary statistics of P10/P1 ratios in the GPe subregions under basal state (left) (one-way ANOVA with two-sided Holm-Sidak's post-hoc multiple comparisons test; $p < 0.0001$) and before and after bath application of quinpirole (right) (repeated measures two-way ANOVA with two-sided Holm-Sidak's post-hoc multiple comparisons test; QP treatment, $p = 0.0004$, GPe subregions, $p < 0.0001$, interaction, $p = 0.2442$). **n**, Summary statistics of charge ratios in the GPe subregions (left) (one-way ANOVA with two-sided Holm-Sidak's post-hoc multiple comparisons test; $p = 0.0389$) and between the GPe subgroups (right) (n (cells/mice): DL-VM GPe (32/28), VL-DM GPe (31/27), two-tailed unpaired t-test; $p = 0.0066$). The data are presented as box-and-whisker plots (center line, median; box limits, 25th and 75th percentiles; whiskers, minimum to maximum values) or mean ± SEM. *$p < 0.05$, **$p < 0.01$, ***$p < 0.001$, ****$p < 0.0001$.

Fig. 6 | DA depletion reshapes the region-specific dopaminergic modulation of striatopallidal synaptic transmission

a, Illustration describing the unilateral injection of 6-OHDA into the MFB (left) and optogenetic recording of striatopallidal transmission (right). **b-e**, Illustrations of the GPe subregions (top left), representative recording traces (bottom left), oIPSC amplitude (top center) and PPR plots (bottom center) normalized to the baseline during bath application of quinpirole (10 μM), and summary statistics of normalized oIPSCs (top right) and normalized PPRs (bottom right) in the DA-depleted condition. Ipsilateral (6-OHDA-lesioned) data are indicated in blue, while contralateral data are shown in black. Red bars and labels indicate the quinpirole application state. Summary statistics of normalized oIPSCs (n (cells/mice): DL contra (17/15), DL ipsi (16/14), VL contra (14/12), VL ipsi (15/12), DM contra (11/11), DM ipsi (12/12), VM contra (15/12), VM ipsi (18/16), two-tailed one-sample t-test; DL QP ON, $p < 0.0001$, DL QP OFF, $p < 0.0001$, VL QP ON, $p < 0.0001$, VL QP OFF, $p < 0.0001$, DM QP ON, $p < 0.0001$, DM QP OFF, $p < 0.0001$, VM QP ON, $p < 0.0001$, VM QP OFF, $p < 0.0001$) and normalized PPRs (DL QP ON, $p = 0.0752$, DL QP OFF, $p = 0.2478$,

VL QP ON, p = 0.0014, VL QP OFF, p = 0.0002, DM QP ON, p = 0.0015, DM QP OFF, p = 0.0069, VM QP ON, p = 0.0043, VM QP OFF, p = 0.0566) in the GPe subregions. **f,g,** Summary statistics of the normalized PPRs between hemispheres during QP ON state (n (cells/mice): DL contra (17/15), DL ipsi (16/14), VL contra (14/12), VL ipsi (15/12), DM contra (11/11), DM ipsi (12/12), VM contra (15/12), VM ipsi (18/16), two-tailed unpaired t-test; DL, p = 0.0381, VL, p = 0.0424, DM, p = 0.0055, VM, p = 0.0343) and QP OFF state (DL, p = 0.0055, VL, p = 0.0041, DM, p = 0.0167, VM, p = 0.5667) in the GPe subregions. The data are presented as box-and-whisker plots (center line, median; box limits, 25th and 75th percentiles; whiskers, minimum to maximum values) or mean ± SEM. *p < 0.05, **p < 0.01, ***p < 0.001, ****p < 0.0001.

Fig. 7 | DA depletion induces region-specific alterations in the spatial distribution of presynaptic D2Rs at striatopallidal axon terminals

a, A schematic illustration depicting the injection of AAV5-hSyn-Flex-mGFP-2A-Synaptophysin-mRuby virus into the striatum of Adora2A-Cre mice, along with the unilateral injection of 6-OHDA into the MFB. **b**, Representative enhanced confocal images of striatopallidal axon terminals and D2Rs in the GPe subregions of the contralateral and ipsilateral (6-OHDA) hemispheres. **c,d,** Summary statistics of D2R+ area (n (images/mice): contra DL-VM GPe (118/11), contra VL-DM GPe (120/11), ipsi DL-VM GPe (120/11), ipsi VL-DM GPe (120/11), two-tailed unpaired t-test; contra, p < 0.0001, ipsi, p = 0.6068), D2R+ area colocalized with RFP+ area (contra, p < 0.0001, ipsi, p = 0.0687), D2R+ area colocalized with GFP+ area (contra, p = 0.0093, ipsi, p = 0.2801), and D2R+ area colocalized with GFP+ or RFP+ area (contra, p < 0.0001, ipsi, p = 0.0263) between GPe subgroups and hemispheres. **e,f,** Edge-corrected Ripley's H function analysis of the distance from RFP to D2R in the DL-VM GPe and VL-DM GPe (null model, CE: confidence envelope) (left), and the distance from RFP to D2R in the VL-DM GPe and DL-VM GPe (null model, CE: confidence envelope) (right) between hemispheres. **g**, Summary statistics of D2R+ area (left) (ordinary two-way ANOVA with two-sided Holm-Sidak's post-hoc multiple comparisons test; GPe subgroup, p = 0.0023, 6-OHDA, p = 0.4646, interaction, p = 0.0023) and D2R+ area colocalized with RFP+ area (right) (GPe subgroup, p = 0.0020, 6-OHDA, p = 0.0032, interaction, p = 0.6695) comparing the contralateral and ipsilateral hemispheres. **h**, Edge-corrected Ripley's H function analysis of the distance from RFP to D2R in the ipsilateral GPe and

contralateral GPe (null model, CE: confidence envelope) (left), the distance from RFP to D2R in the DL-VM GPe (center) and VL-DM GPe (right) of the ipsilateral hemisphere and contralateral hemisphere. Rejection rate of the distance from RFP to D2R in the ipsilateral hemisphere, evaluated using the DCLF test (compared to the null model of the contralateral hemisphere) (right). The data are presented as box-and-whisker plots (center line, median; box limits, 25th and 75th percentiles; whiskers, minimum to maximum values), mean ± SEM or bar graph. *$p < 0.05$, **$p < 0.01$, ****$p < 0.0001$.

Fig. 8 | Computational modeling of striatopallidal synapses indicates region-specific changes in calcium dynamics

a, A schematic illustration depicting the mathematical framework of computational modeling at striatopallidal synapses. **b**, Representative simulated PPR traces of GPe subregions under control conditions (Control) and DA-depleted conditions (6-OHDA). **c-f**, Schematic illustrations of the GPe subregions (left), summary statistics of simulated Ca^{2+} channel open probability (middle), and Ca^{2+} concentration at the axon terminals (right) under control conditions (n (models): 10 per GPe subregion, two-tailed Wilcoxon matched pairs signed rank test). **c**, Summary statistics of simulated Ca^{2+} channel open probability ($p = 0.002$) and Ca^{2+} concentration ($p = 0.002$) in the DL GPe. **d**, Summary statistics of simulated Ca^{2+} channel open probability ($p = 0.4316$) and Ca^{2+} concentration ($p = 0.3223$) in the DM GPe. **e**, Summary statistics of simulated Ca^{2+} channel open probability ($p = 0.2324$) and Ca^{2+} concentration ($p = 0.2227$) in the VL GPe. **f**, Summary statistics of simulated Ca^{2+} channel open probability ($p = 0.002$) and Ca^{2+} concentration ($p = 0.002$) in the VM GPe. **g-j**, Schematic illustrations of the GPe subregions (left), summary statistics of simulated Ca^{2+} channel open probability (middle), and Ca^{2+} concentration at the axon terminals (right) under DA-depleted conditions (n (models): DL (9), VL (9), DM (9), VM (17), two-tailed Wilcoxon matched pairs signed rank test). **g**, Summary statistics of simulated Ca^{2+} channel open probability ($p = 0.1641$) and Ca^{2+} concentration ($p = 0.1523$) in the DL GPe. **h**, Summary statistics of simulated Ca^{2+} channel open probability ($p = 0.0078$) and Ca^{2+} concentration ($p = 0.0078$) in the DM GPe. **i**, Summary statistics of simulated Ca^{2+} channel open probability ($p = 0.0039$) and Ca^{2+} concentration ($p = 0.0039$) in the VL GPe. **j**, Summary statistics of simulated Ca^{2+} channel open probability ($p < 0.0001$) and Ca^{2+} concentration ($p < 0.0001$) in the VM GPe. The data are presented as box-and-

whisker plots (center line, median; box limits, 25th and 75th percentiles; whiskers, minimum to maximum values). **$p < 0.01$, ****$p < 0.0001$.

Editor's summary:

Whether dopaminergic modulation of synaptic transmission can vary by the anatomical location of striatopallidal synapses in the GPe (external globus pallidus) is not fully understood. Here authors demonstrate that dopamine fine-tunes striatopallidal synaptic transmission by acting on presynaptic D2 and postsynaptic D4 receptors across subregions of the GPe. In addition, dopamine depletion reshapes this modulation in the opposite direction.

Peer review information: *Nature Communications* thanks the anonymous reviewer(s) for their contribution to the peer review of this work. A peer review file is available.

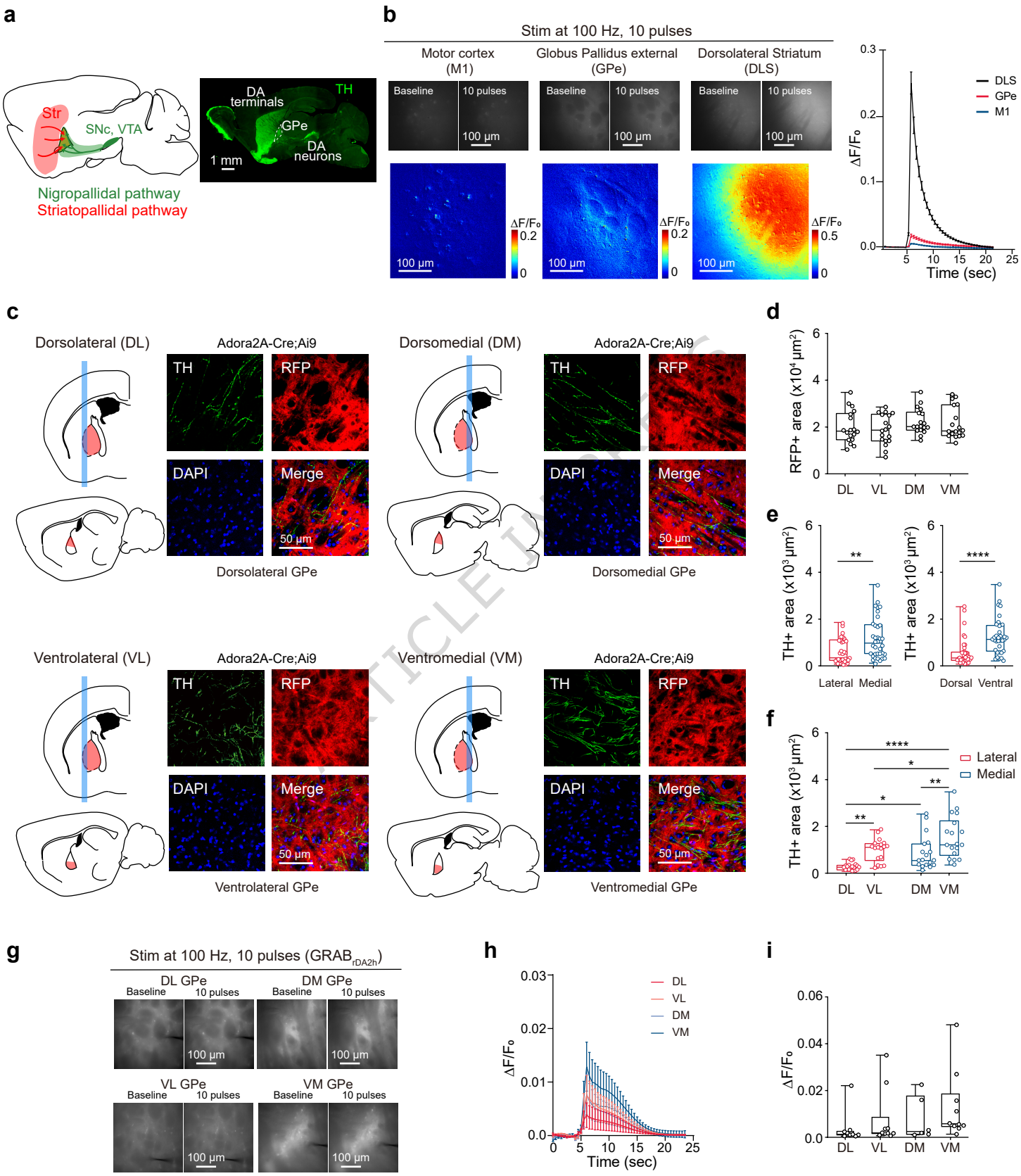
a
Str
SNc, VTA
Nigropallidal pathway
Striatopallidal pathway
DA terminals
TH
GPe
DA neurons
1 mm
b
Stim at 100 Hz, 10 pulses
Motor cortex (M1)
Globus Pallidus external (GPe)
Dorsolateral Striatum (DLS)
Baseline
10 pulses
100 µm
ΔF/Fo
DLS
GPe
M1
Time (sec)
c
Dorsolateral (DL)
Dorsomedial (DM)
Ventrolateral (VL)
Ventromedial (VM)
Adora2A-Cre;Ai9
TH
RFP
DAPI
Merge
50 µm
Dorsolateral GPe
Dorsomedial GPe
Ventrolateral GPe
Ventromedial GPe
d
RFP+ area (x10⁴ µm²)
DL
VL
DM
VM
e
TH+ area (x10³ µm²)
Lateral
Medial
Dorsal
Ventral
f
TH+ area (x10³ µm²)
Lateral
Medial
g
Stim at 100 Hz, 10 pulses (GRAB rDA2h)
h
ΔF/Fo
Time (sec)
i
ΔF/Fo

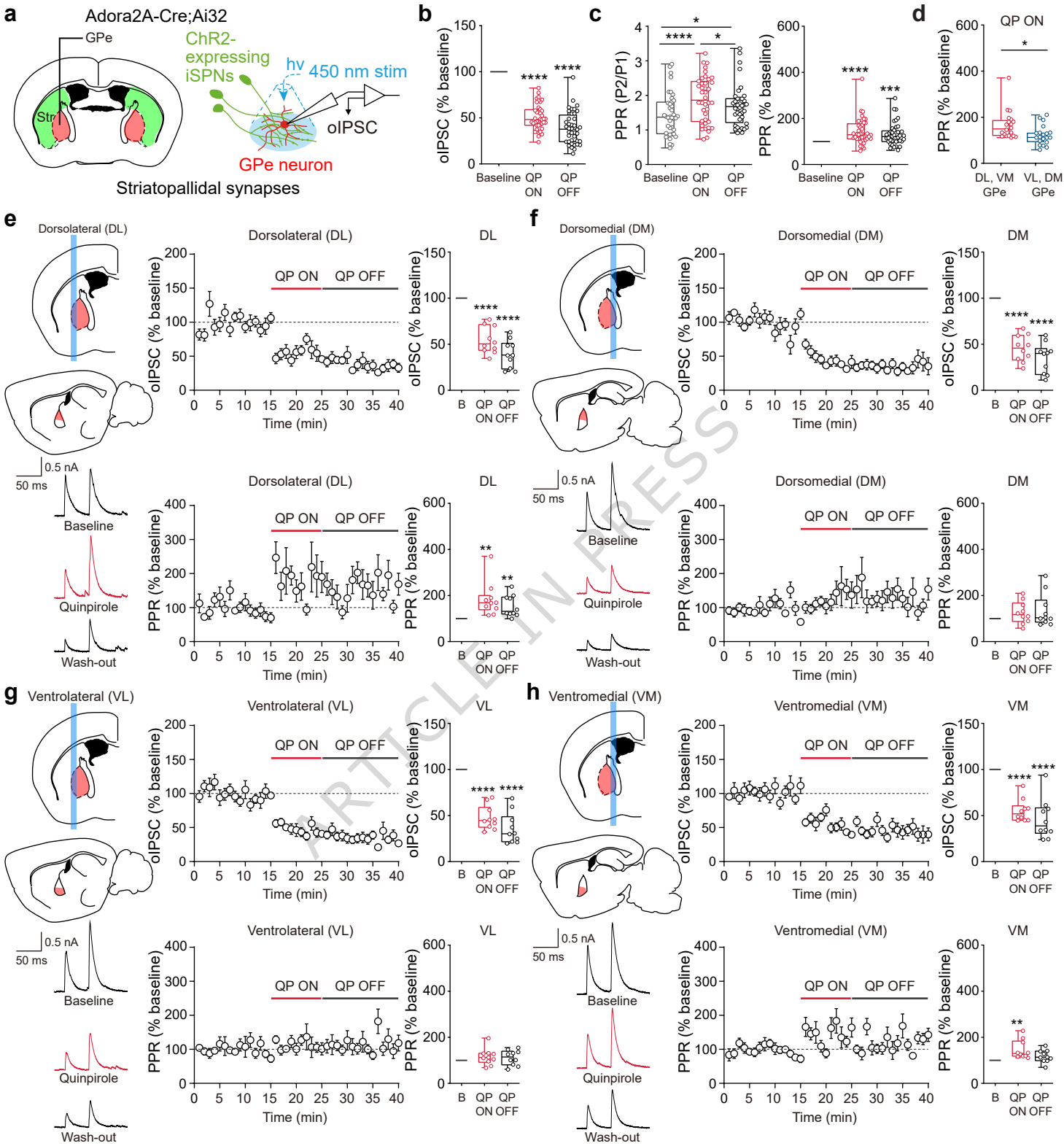

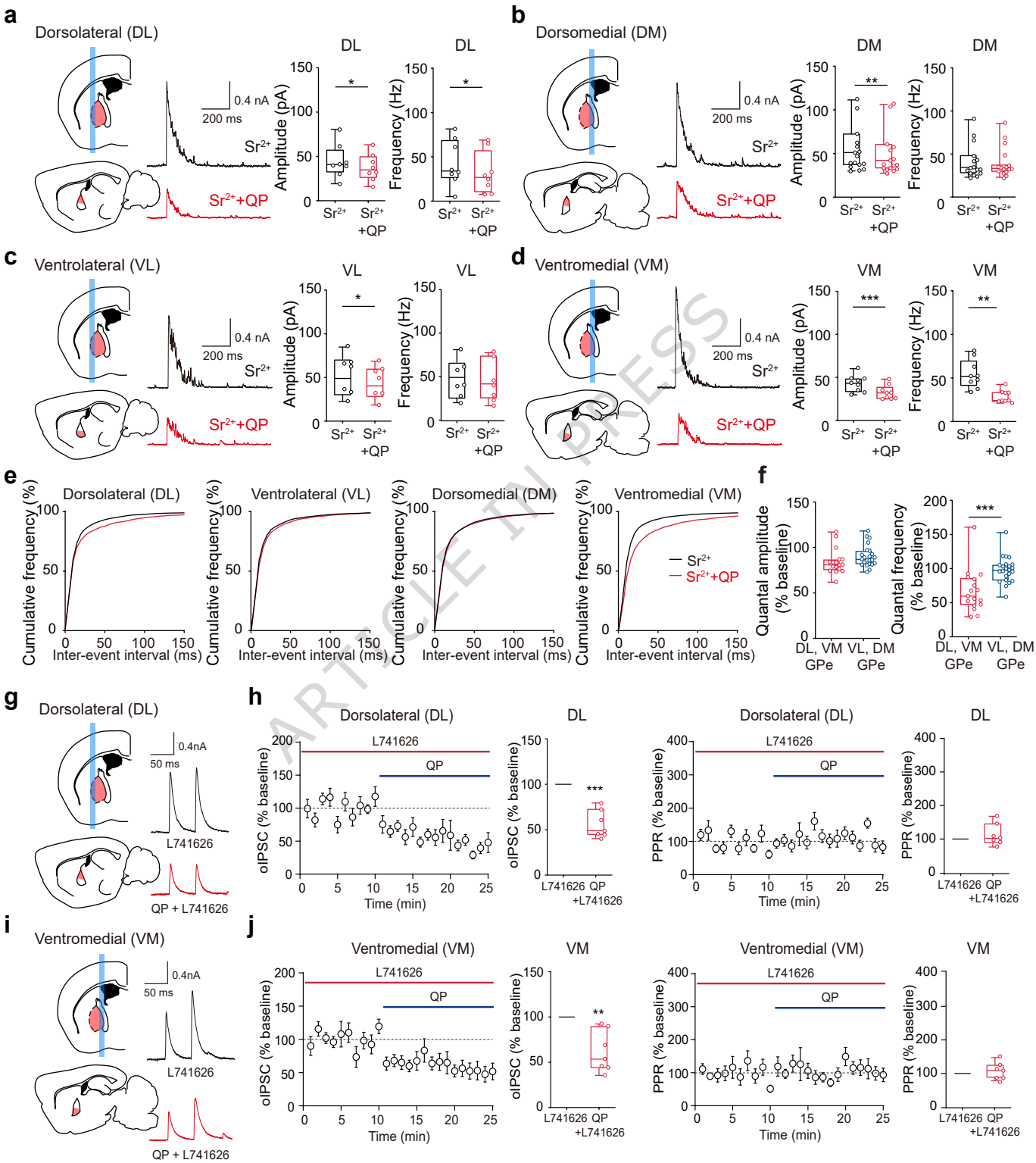

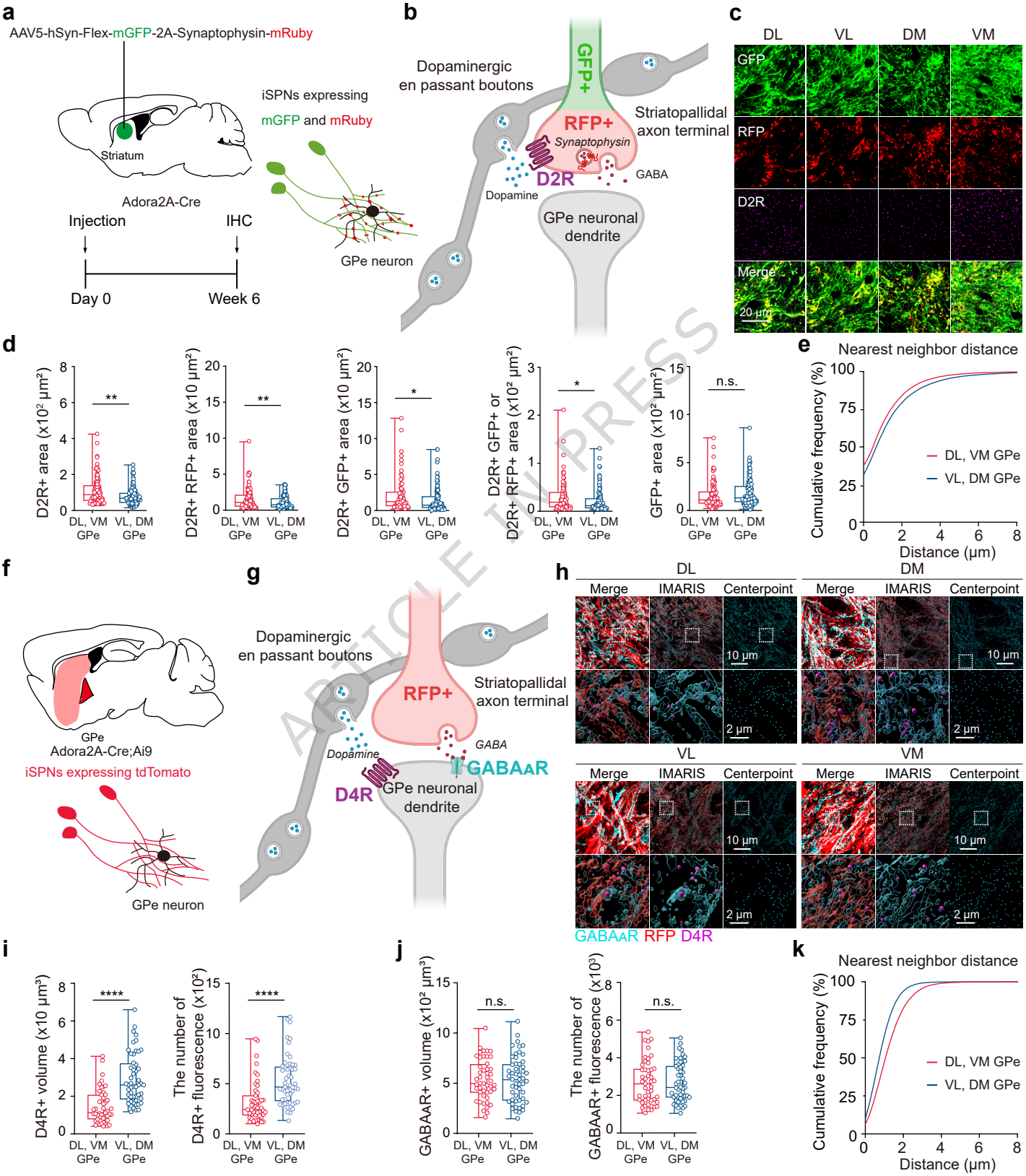
a
AAV5-hSyn-Flex-mGFP-2A-Synaptophysin-mRuby
Striatum
iSPNs expressing
mGFP and mRuby
Adora2A-Cre
Injection
IHC
Day 0
Week 6
GPe neuron
b
Dopaminergic
en passant boutons
GFP+
RFP+
Synaptophysin
Striatopallidal
axon terminal
D2R
Dopamine
GABA
GPe neuronal
dendrite
c
DL
VL
DM
VM
GFP
RFP
D2R
Merge
20 μm
d
D2R+ area (x10² μm²)
D2R+ RFP+ area (x10 μm²)
D2R+ GFP+ area (x10 μm²)
D2R+ GFP+ or
D2R+ RFP+ area (x10² μm²)
GFP+ area (x10² μm²)
**
**
*
*
n.s.
DL, VM
GPe
VL, DM
GPe
e
Nearest neighbor distance
Cumulative frequency (%)
DL, VM GPe
VL, DM GPe
Distance (μm)
f
GPe
Adora2A-Cre;Ai9
iSPNs expressing tdTomato
GPe neuron
g
Dopaminergic
en passant boutons
RFP+
Striatopallidal
axon terminal
Dopamine
GABA
GABAAR
D4R
GPe neuronal
dendrite
h
DL
DM
VL
VM
Merge
IMARIS
Centerpoint
10 μm
2 μm
GABAAR RFP D4R
i
D4R+ volume (x10 μm³)
The number of
D4R+ fluorescence (x10²)
****
****
DL, VM
GPe
VL, DM
GPe
j
GABAAR+ volume (x10² μm³)
The number of
GABAAR+ fluorescence (x10³)
n.s.
n.s.
k
Nearest neighbor distance
Cumulative frequency (%)
DL, VM GPe
VL, DM GPe
Distance (μm)